LITHOS 488–489 (2024) 107824

Contents lists available at ScienceDirect

LITHOS

journal homepage: www.elsevier.com/locate/lithos

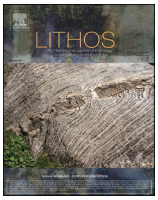

Polymetamorphism and metastability in Paleozoic schists of the central Appalachian Baltimore Terrane, USA

Freya R. George [a,b,*], Daniel R. Viete [b], George L. Guice [c], Kayleigh M. Harvey [d,e], Stephanie Walker [e], Ethan F. Baxter [e]

[a] *School of Earth Sciences, Wills Memorial Building, University of Bristol, Queens Road, Bristol BS8 1RJ, UK*
[b] *Department of Earth & Planetary Sciences, Olin Hall, Johns Hopkins University, Baltimore, MD 21218, USA*
[c] *Department of Physics, Astronomy and Geosciences, Towson University, 8000 York Road, Towson, MD 21252, USA*
[d] *JEOL USA, Inc., 11 Dearborn Rd., Peabody, MA, USA*
[e] *Earth and Environmental Sciences, Devlin Hall, Boston College, 140 Commonwealth Avenue, Chestnut Hill, MA 02467, USA*

ARTICLE INFO

Keywords:
Garnet
Sm–Nd geochronology
Phase equilibria modelling
Polymetamorphism
Metastability
Appalachian

ABSTRACT

Metapelitic assemblages are often considered highly reactive during prograde metamorphism, such that they effectively record a history of tectono-metamorphic processes. Across eastern North America, metamorphosed rift-to-drift stratigraphy has been central to disentangling the terminal history of Appalachian convergence. We report results from a single metapelitic outcrop in the Loch Raven Schist of Maryland's Baltimore Terrane, where regional metamorphism is historically interpreted to have derived only from the Ordovician Taconic orogeny. An aluminum-rich litho-horizon alludes to two phases of metamorphism: an early, low/medium-pressure (*P*) sillimanite-stabilizing phase largely overprinted by a subsequent medium/high-*P* kyanite-stabilizing event, terminating at c. 391–383 Ma. This provides evidence of substantial crustal disturbances in the central Appalachians during Avalonian collision of comparable timing to equivalent events in the north. In a subordinate and aluminum-poor litho-horizon, large (2–3.5 cm) garnet provides geochronological evidence only for a protracted phase of metamorphism at 440–424 Ma. We interpret this age as recording the early, low/medium-*P* phase of metamorphism that either: (a) extends the duration of the Taconic event; or (b) provides new evidence for metamorphism associated with Silurian tectonism and/or extension in the Central Appalachians. However, this assemblage appears to have been metamorphically unresponsive during Devonian overprinting, despite peak metamorphic conditions of ~670 °C and ~8 kbar. We suggest that a potential combination of the paucity of fluid, limited strain accumulation, and coarse refractive assemblages stabilized a kinetically sluggish and metastable composition.

1. Introduction

Rocks of the North American Appalachians preserve a protracted history of Paleozoic convergence. Cambrian–Ordovician subduction initiation was followed by staggered accretion of terranes to the Laurentian margin—including Acadian-phase (late Silurian to mid Devonian) collision of Avalonia in the northern Appalachians—and widespread Alleghenian suturing to assemble Pangea during the Carboniferous to mid-Permian (e.g., see Hibbard et al., 2010; Fig. 1a). The post-Ordovician architecture produced by this convergence differs along strike, but much of the core of the orogen comprises a belt of Mesoproterozoic Laurentian (Grenvillian) basement inliers (e.g., Volkert and Aleinikoff, 2021). Cover sequences of metasedimentary clastic and carbonate rocks atop these domed gneisses provide a record of the convergent history (e.g., Hibbard, 1994; Hughes et al., 2014; Macdonald et al., 2014).

In the northern Appalachians, this cover sequence has been the focus of foundational petrological, geochronological, and structural studies (e.g., Spear et al., 2002). However, equivalent studies are less common in the central Appalachians of Virginia, Maryland, Pennsylvania, and New Jersey, where the rocks are less well exposed. In central Maryland's Baltimore Terrane, metamorphism and deformation is generally interpreted to be product of the Taconic Orogeny, which involved Ordovician collision between a peri-Laurentian arc and the Laurentian margin at

---

* Corresponding author at: School of Earth Sciences, Wills Memorial Building, University of Bristol, Queens Road, Bristol BS8 1RJ, UK.
E-mail address: freya.george@bristol.ac.uk (F.R. George).

https://doi.org/10.1016/j.lithos.2024.107824
Received 16 May 2024; Received in revised form 16 September 2024; Accepted 20 September 2024

460–455 Ma (Aleinikoff et al., 2006; Lang, 1991; Sinha et al., 2012; Wagner and Srogi, 1987; Wise and Ganis, 2009). Relative to the northern Appalachians, where (a) Late Silurian to early Devonian Acadian-phase orogenesis (423–385 Ma in Robinson et al., 1998; 425–400 Ma in van Staal et al., 2009) is characterized by west- and east-verging nappes, widespread syn-tectonic magmatism, and regional amphibolite facies metamorphism, and (b) exposure of peri-Gondwanan terranes (Avalonia, Meguma, Ganderia) is significant (Fig. 1a), evidence of Acadian-phase tectonism remains limited in the central Appalachians (Bosbyshell et al., 2016). Acadian-phase tectonics and metamorphism are thus generally considered to have played a minor role in the Appalachian convergent history south of New England (e.g., Dennis and Wright, 1997; Trupe et al., 2003).

In this study, we present results of detailed petrography, geochemical analyses, thermobarometry, and garnet Sm–Nd geochronology for two metapelite samples from a single outcrop of the Loch Raven Schist, a metasedimentary unit high in the stratigraphy of the cover sequence of the Baltimore Terrane. The constraints presented in this paper suggest that the region experienced a prolonged, polymetamorphic evolution, involving: (a) initial low/medium-pressure metamorphism that peaks at c. 424 Ma and which is cryptically preserved, and (b) secondary, more widely recorded, higher-pressure Acadian (c. 383 Ma) prograde history. These represent the first constraints on the tectono-metamorphic evolution of the Loch Raven Schist in Maryland and provide unequivocal evidence that Acadian orogenesis in the central Appalachians drove medium–high grade metamorphism. The heterogeneity in geochronological results derived from these rocks demonstrate that metapelitic assemblages that experience a complex multistage reaction–dehydration history can remain metamorphically unresponsive and metastable even at near-solidus conditions.

2. Geological background

The Appalachians are commonly separated into northern, central, and southern segments. Each is considered distinct with respect to protolith age, lithology, and tectono-metamorphic history (Bosbyshell et al., 2016; Hatcher et al., 2010; Hibbard et al., 2007; Rodgers, 1970; Sinha et al., 2012). Across strike, three tectonic domains are defined, from west to east: (a) the Laurentian margin; (b) the Iapetan realm (often known as the Piedmont; Hibbard et al., 2007), and (c) the Peri-Gondwanan realm (Fig. 1a). Together, these record a protracted history of ocean closure (the Iapetus and Rheic Oceans), and associated orogenic, magmatic and sedimentary events. In the US state of Maryland, Neoproterozoic and Paleozoic rocks of the Piedmont are divided, from west to east, into: (a) the Frederick Valley synclinorium; (b) the Sugarloaf Mountain anticlinorium; (c) the Westminster Terrane; (d) the Potomac Terrane, and (e) the Baltimore Terrane (Fig. 1b).

In Maryland's eastern Piedmont, c. 1.25 Ga Grenvillian gneiss domes of the Baltimore Terrane are unconformably overlain by a sedimentary succession that is locally grouped as the Glenarm Supergroup (Crowley, 1976). The Glenarm Supergroup records a depositional history that fines upwards from sandstone to shale (Setters Formation), transitioning to carbonates (Cockeysville Marble) and then to fine-grained clastics (Loch Raven Schist), graywackes (Oella Schist and Piney Run Formation), and diamictite (Sykesville Formation; Fig. 1b). The Glenarm Supergroup is interpreted to record the rift-to-drift (Setters Formation and Cockeysville Marble) evolution of the Iapetan margin during the latest Neoproterozoic to earliest Cambrian (Fisher and Higgins, 1979; Fisher and Olsen, 2004), followed by initiation of convergence, tectonic downflexure of the margin, and *syn*-convergent (foredeep) deposition of clastic units during the Ordovician (Loch Raven Schist and overlying metagraywackes and diamictite; Crowley, 1976). The Loch Raven Schist and overlying units are generally considered the Baltimore-area equivalent of the Wissahickon Formation/Schist of Pennsylvania, New Jersey and Delaware (Crowley, 1976).

Samples investigated in this study are derived from the Loch Raven Schist, a ~600 m-thick sequence of metapelitic schists, phyllites and metagraywackes, with local psammitic layers. In Baltimore, the Loch Raven Schist has a maximum depositional age of c. 530 Ma (Martin and Bosbyshell, 2019). Detrital zircon geochronology suggests that upper Glenarm Supergroup sediments in the Potomac and Westminster Terranes (the Piney Run Formation and the Prettyboy Schist) are exclusively Laurentian derived (Martin and Bosbyshell, 2019). However, the Setters Formation in Baltimore has yielded only Laurentian detrital zircon populations, whereas the type-Wissahickon Schist in Pennsylvania has yielded Precambrian, Laurentian-associated, and Ediacaran (interpreted as Gondwanan-associated) zircon populations (Bosbyshell et al., 2015). Moreover, the presence of both 670–580 Ma and

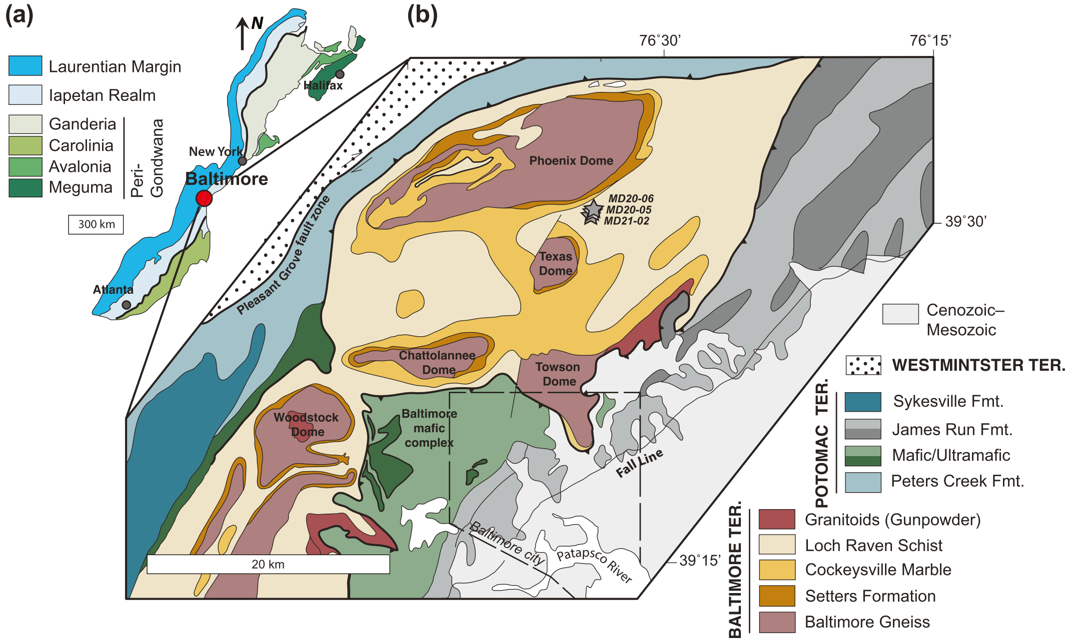

Fig. 1. (a) Simplified lithostratigraphic map of Appalachian orogen in the United States and Canada. (b) Simplified geological map of the Baltimore Terrane, including samples collected as part of this study (stars). Redrawn after Kavage-Adams et al. (2020). Abbreviations: Fmt. = Formation. Ter. = Terrane.

1150–980 Ma detrital zircon age populations in the Loch Raven Schist has been taken to suggest contribution of both Laurentian- and Gondwanan-derived sediments (Martin and Bosbyshell, 2019).

Unlike in the Pennsylvania–Delaware Piedmont, where metamorphic grade increases approximately monotonically from northwest to southeast (Alcock, 1989), greenschist- to amphibolite-facies isograds in the Maryland Piedmont are spatially associated with basement gneisses (Fig. 1b; e.g., Olsen, 1977): metamorphic grade within the cover sequence increases toward the gneiss domes. The domes and isograd pattern in their cover sequence are considered a result of interference between nappe structures along a regional décollement and late (post-metamorphic) upright folds (Fisher and Olsen, 2004). Previous estimates of metamorphic conditions recorded by the Setters Formation along the southern margin of the Phoenix Dome suggest the Baltimore Terrane reached 590–616 °C at 6–6.5 kbar (Lang, 1991, 1996). No pressure–temperature (*P*–*T*) constraints have been published for the Loch Raven Schist.

Constraints on the timing of amphibolite facies metamorphism recorded in the Baltimore Terrane are limited, and commonly ascribed to the c. 453 Ma (Taconic) orogenesis documented in zircons of the Baltimore Mafic Complex (BMC; Sinha et al., 1997; Sinha et al., 2012). Unlike in the Northern Appalachians, Devonian (Acadian) tectonism is generally thought to have had minimal impact on the rocks exposed in the central Appalachians (e.g., Hibbard et al., 2010). However, there is increasing evidence to suggest that this may not be the full picture. Bosbyshell et al. (2007) suggested that in southern Pennsylvania, oblique convergence along the Rosemount Shear Zone at 425–385 Ma (Th-U-Total Pb monazite) led to moderate pressure metamorphism (Bosbyshell et al., 2016). Similarly, ^{40}Ar/^{39}Ar of low-grade phases in the rocks from the Westminster and Potomac Terranes of Maryland, Pennsylvania and Virginia allude to early Silurian and Devonian cleavage formation (Wintsch et al., 2010), and metamorphic zircon and monazite U–Pb ages in samples from northern Delaware point to granulite facies metamorphism at c. 426–438 Ma (Aleinikoff et al., 2006; Srogi et al., 1993; Srogi and Lutz, 1997). The timing and nature (polymetamorphic or not) of the widespread metamorphism recorded in the Baltimore Terrane therefore remains very poorly understood. There are no published garnet age data available from the Baltimore Terrane which would unambiguously constrain the timing of prograde to peak metamorphism.

3. Petrography and geochemistry of key samples

This study focuses on several samples of Loch Raven Schist collected in suburban parkland along Overshot Run, near to the local kyanite-in isograd of Crowley (1976). At the sampling locality, the lithology represented by MD21–02 and MD20–05 are well-exposed (Fig. 2). These rocks are representative of the major regional lithology of the Loch Raven Schist along the northeast margin of the Texas Dome. The lithology sampled as MD20–06 is more poorly exposed, confined in a foliation-parallel layer, the lateral and stratigraphic extent of which cannot be determined owing to local exposure being mostly limited to creek beds. The present mineralogical contact between the two assemblages is sharp (Fig. 2b). There is no evidence for localized deformation, lithological/metamorphic telescoping, or fluid flow along the lithological boundary that separates sampled equivalent to MD20-–06 from samples equivalent to MD21–02 and MD20–05.

3.1. Analytical methodologies

Quantitative major element analyses and garnet traverses were performed using a JEOL JXA-8530F electron probe microanalyzer (EPMA) equipped with five wavelength dispersive spectroscopy (WDS) detectors at the Smithsonian Institution's National Museum of Natural History (Department of Mineral Sciences). The accelerating voltage was set to 20 kV, beam current to 10 nA, analyses used a 1 μm spot diameter, and on- and off-peak counting times were 30 s and 15 s, respectively. Calibration was to a suite of Smithsonian standards, with secondary standards analyzed before and after each session to assess the accuracy of analyses; all standard and unknown data are provided in Supplementary Material 2. All analyses were processed using a ZAF correction scheme. The raw EPMA data were recalculated to element oxide percentages, with Fe^{2+} and Fe^{3+}calculated using the charge balance method of Schumacher (1991). Garnet EPMA maps were acquired using an accelerating voltage of 15 kV, a beam current of 200 nA, and a 5 μm beam diameter.

Bulk rock major element analyses were performed on glass discs produced by flux melting of whole-rock powders in the presence of lithium tetraborate. 253 g and 1.3 kg of MD21–02 and MD20–06, respectively, were powdered for this purpose. X-ray fluorescence (XRF) analysis of the glass discs was performed at the Department of Earth and Environmental Sciences, Franklin and Marshall College, using a PANanalytical 2404 XRF spectrometer.

To assess the spatial distribution of trace elements, laser ablation raster mapping and spot analyses of garnet were conducted in the Department of Earth & Planetary Sciences, Johns Hopkins University. Analyses were performed using a Teledyne Cetac Analyte G3 193 nm excimer LA system with a Helex II 2-volume ablation cell coupled to an Agilent 8900 triple quadrupole ICP-MS via PEEK tubing. For the c. 3 cm garnet from MD20–06, parallel raster line scans used a 100 × 100 μm square aperture, a 100 Hz repetition rate, and a fluence of 2.6 J/cm^2. To synchronize the pulse frequency and ICP-MS duty cycle and minimize

Fig. 2. (a) Site of key sampling as part of this study. Exposure of overlying MD21–02 (blue), and MD20–06 (red) below, with curved lines illustrating overall fabric in shadows. (b) Contact between two sample lithologies, denoted by a dashed line and most evident in garnet porphyroblast size, highlighted in red and blue. (For interpretation of the references to colour in this figure legend, the reader is referred to the web version of this article.)

aliasing, a scan speed of 1000 μm/s was used. Ablation was performed in a He carrier gas (0.575 mL min^{-1}) mixed downstream with Ar (1.3 L min^{-1}). In the case of smaller garnets from MD21–02, laser aperture was 25 × 25 μm, repetition rate was 90 Hz, and fluence was 2 J/cm^2. Scan speed was 140 μm/s. All other analytical conditions were the same for MD20–06. For both samples, each line scan was followed by 10 s of washout. For core-to-rim profiles, each individual 40 × 40 μm trace element spot in garnet comprised 200 shots with fluence of 3 J/cm^2 at repetition rate of 10 Hz. Bulk rock trace element abundance was determined by analyzing glasses produced at Franklin and Marshall College for XRF major element analyses. Line rasters 600 μm-long were run over glasses with a 50 × 50 μm square beam aperture and with a laser fluence of 3 J/cm^2 at 10 Hz and 10 μm/s.

Spot data processing and integrated line scans (on both garnet and glass) were generated offline using the internally standardized 'Trace Element' reduction scheme included in iolite v4 (Hellstrom et al., 2008; Paton et al., 2011). Quantification of laser data was completed using the measured (by EPMA) average value of Si in garnet (for garnet) and using ^{43}Ca independently determined with XRF (for glasses) and an internal NIST612 standard reference material. Periodic raster line scans along NIST610 were used as an additional check on data quality.

3.2. Samples MD21–02 and MD20–05

Samples MD21–02 and MD20–05 are highly aluminous metapelites that represent the predominant assemblage in the Loch Raven Schist to the northwest of the Texas Dome (Fig. 3). Bulk rock compositions are presented in Table 1 and Supplemental Material 1. In addition to high Al_2O_3, the rocks have relatively high Zr (230–300 ppm) and low Cr content (<15 ppm). Bulk Nd and Sm are ~80 ppm and ~ 15 ppm, respectively.

Both MD21–02 and MD20–05 contain an assemblage of sillimanite (1–2 vol%), kyanite (6–9 vol%), staurolite (< 5 vol%), garnet (13–22 vol %), muscovite (15–16 vol%), biotite (~15–20 vol%), plagioclase and quartz (20–37 %), ilmenite (2–3 vol%), apatite, and tourmaline, with accessory monazite and zircon. Phase analyses of MD21–02 are presented in Table 2, with MD20–05 in Supplementary Material 2. Samples contain biotite that define two populations: low Ti (0.19–0.23 cpfu) and high Ti (0.25–0.31 cpfu). No clear spatial or textural relationships can be assigned to the two biotite populations in either sample. Plagioclase inclusions in garnet have X_{An} 0.44–0.52, and matrix plagioclase have X_{An} of ~0.3. Secondary chlorite is present in the matrix of both samples.

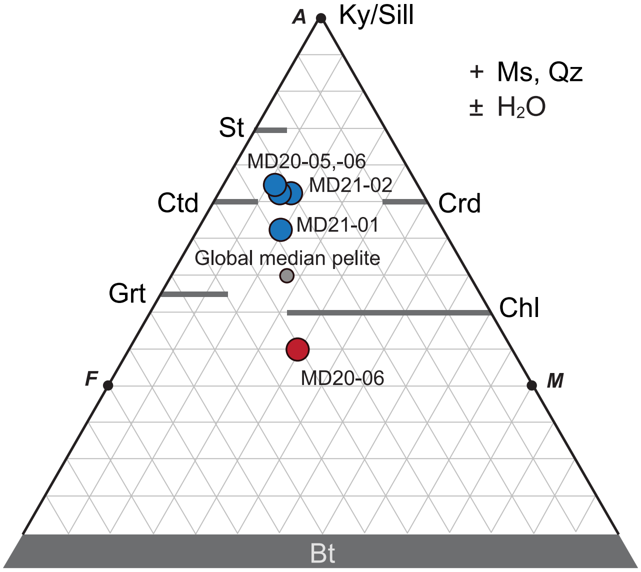

Fig. 3. AFM diagram showing bulk compositions of samples. Bulk rock composition of global median pelite determined by Forshaw and Pattison (2023) is also plotted.

The 2–5 mm subhedral garnets in samples MD21–02 and MD20–05 have pronounced core and rim zones (Fig. 4a). The cores contain randomly orientated inclusions of sillimanite and fibrolite mats, highly rounded quartz, ilmenite, biotite, apatite, tourmaline, white mica, and staurolite (Fig. 4b, c). Core regions also contain crystallographically aligned fluid inclusions (Fig. 4c), making the garnet appear 'cloudy'; these inclusions are absent in zones around coarser inclusions of sillimanite, quartz, and ilmenite, and are therefore interpreted as having formed by secondary internal metasomatic processes, as discussed by Dempster et al. (2019). The 200–500 μm wide rims of garnet contain few inclusions, but notably, contain inclusions of external foliation-aligned sillimanite (Fig. 4a, b).

Staurolite forms both coarse euhedral (~3 mm) and ragged porphyroblasts in the matrix (Fig. 4b). Kyanite principally overgrows biotite-rich cleavage domains and forms a sporadically developed mineral lineation evident in outcrop (Fig. 4a). In many places, kyanite rims are also ragged. In addition to unaligned sillimanite inclusions in garnet cores and foliation-aligned sillimanite included in garnet rims, sillimanite takes several other forms: (a) as inclusions in euhedral–subhedral staurolite that are aligned with the external fabric (Fig. 4d); (b) directly replacing kyanite (Fig. 4g), and (c) as fibrolite mats intergrown with muscovite and/or quartz (Fig. 4d, e). The latter is interpreted to record a retrograde reaction.

Garnet chemical zoning

Major element zoning in garnet from MD21–02, representative also of MD20–05, is summarized in the maps and profiles of Fig. 5a and b. Garnets have semi-concentric major element core-to-rim zoning, with diffuse and irregular shaped cores that are enriched in spessartine (7–10 mol%) and grossular (14–16 mol%), and depleted in pyrope (4–5 mol%) and almandine (70–72 mol%) relative to rims. Across steep mantle gradients, spessartine decreases to 1 mol% at garnet rims while pyrope and almandine is relatively enriched (13–14 and 78–82 mol%, respectively) at rims (Fig. 5a). Rimwards of the core, grossular content decreases to 5 mol%, and then increases at the textural transition from inclusion-rich cores to inclusion-poor outer rims (Figs. 4a and 5a and b); Ca is the only major element to exhibit this change. In the secondary-inclusion free regions around primary polycrystalline inclusions (containing, in Fig. 5b, ilmenite and plagioclase) the grossular and spessartine content is reduced, and pyrope and almandine content is enriched relative to the inclusion's position from core-to-rim; this can be seen in several garnet profiles from both MD20–05 and MD21–02 (Fig. 5a).

LA-ICP-MS maps of the trace element distribution in garnet are presented in Fig. 6 and Supplementary Material 3. Spatially coincident with the maximum spessartine content (Fig. 6a), heavy rare earth elements (HREE) are enriched in garnet cores, in narrow, steep peaks (Fig. 6b, e). Lighter masses are depleted in inner core regions, and MREE–LREE are enriched in a bowl-shape towards mantle regions (Fig. 6c). The Nd concentration across these inclusion-rich core regions is generally 0.17–0.67 ppm (average 0.29 ppm), and Sm (which exhibits more pronounced systematic variation) is 0.49–0.85 ppm (average 0.60 ppm).

Consistent with inclusion density and grossular constraints, trace element zoning supports division of garnets into cores and rims. Chromium, a highly immobile element (George and Gaidies, 2017), best highlights the stepwise transition from cores to rims: a sharp rimwards decrease in Cr content is coincident with a loss of Cr-rich inclusions in the rim (Fig. 6d). Rim-ward of this boundary, heavy to light REE are re-enriched in a position proximal and distal to the discontinuity, respectively (Fig. 6b–f), mimicking typical patterns of prograde REE distribution and partitioning. In the outer rims, the Sm concentration determined by LA-ICP-MS is 1.4–3.2 ppm, and Nd is 0.23–0.63 ppm.

Table 1
X-ray fluorescence data (wt% for oxides, ppm for select trace elements).

Sample	SiO_2	TiO_2	Al_2O_3	FeO*	Fe_2O_3	MnO	MgO	CaO	Na_2O	K_2O	P_2O	LOI	Total	Cr	Zr	V
MD20–06	50.09	2.85	16.38	13.30	2.48	0.14	5.84	2.36	1.12	3.82	0.27	2.07	100.72	159	171	361
MD21–02	52.25	1.16	26.62	8.03	3.00	0.19	1.92	1.66	1.27	2.67	0.25	1.99	101.01	11	186	104
MD20–05	47.17	1.32	30.51	8.54	3.03	0.14	2.42	1.23	1.31	3.21	0.27	2.85	102.00	13	236	116

[*] FeO determined by titration, FeO2- = $Fe_2O_3^T$-FeO*1.111348.

Table 2
Representative mineral compositions (excluding garnet) for sample MD20–06 and MD21–02. Mg = Mg/(Mg + Fe^{2+}), Ti (22O) is the Ti content per 22 oxygen. Inc. = inclusion in garnet; Mtx = in matrix.

Sample	MD20–06							MD21–02					
Mineral	Bt				Pl		Ilm	Bt	Ilm	Pl		Wm	St
Location	Mtx	Inc D	Inc A	Inc E	Mtx	Inc	Mtx + Inc	Mtx	Mtx	Inc	Mtx	Mtx	Mtx
Analyses	35	52	76	61	18	8	5	13	8	4	8	10	
SiO_2	36.03	36.89	35.47	36.31	59.41	58.37	0.02	35.75	0.00	55.31	60.21	46.31	27.86
TiO_2	1.72	1.50	1.82	1.70	0.00	0.00	52.88	1.88	51.78	0.00	0.00	0.97	0.62
Al_2O_3	18.72	17.90	18.17	17.61	25.25	25.70	0.02	19.04	0.02	27.71	24.52	36.06	52.91
FeO	16.98	14.65	18.71	16.86	0.02	0.06	45.20	17.20	46.86	0.16	0.01	1.08	13.37
MnO	0.01	0.01	0.02	0.01	0.01	0.00	0.27	0.00	0.10	0.00	0.02	0.00	0.02
MgO	11.42	12.79	8.58	11.32	0.00	0.00	0.20	11.00	0.31	0.00	0.00	0.71	1.56
CaO	0.02	0.01	0.02	0.01	6.87	7.53	0.01	0.01	0.00	9.82	6.08	0.01	0.01
Na_2O	0.23	0.26	0.09	0.28	7.88	7.61	0.00	0.21	0.00	6.04	7.99	0.51	0.02
K_2O	7.63	7.88	8.72	8.52	0.08	0.07	0.04	8.18	0.03	0.09	0.07	5.61	0.01
Total	92.77	92.01	91.59	92.62	99.54	99.36	98.64	93.26	99.09	99.13	98.90	91.25	96.38
Si	2.73	2.79	2.77	2.78	2.66	2.63	0.00	2.72	0.00	2.51	2.70	3.11	7.88
Ti	0.11	0.10	0.12	0.11	0.00	0.00	1.01	0.11	0.99	0.00	0.00	0.05	0.13
Al_2O_3	1.67	1.60	1.67	1.59	1.33	1.36	0.00	1.71	0.00	1.48	1.30	2.85	17.65
Fe^{2+}	0.88	0.75	1.12	0.91	0.00	0.00	0.96	0.95	0.98	0.01	0.00	0.00	3.05
Fe^{3+}	0.20	0.18	0.10	0.17	0.00	0.00	0.00	0.15	0.02	0.00	0.00	0.06	0.11
Mn	0.00	0.00	0.00	0.00	0.00	0.00	0.01	0.00	0.00	0.00	0.00	0.00	0
Mg	1.27	1.42	1.02	1.28	0.00	0.00	0.01	1.23	0.01	0.00	0.00	0.07	0.66
Ca	0.00	0.00	0.00	0.00	0.33	0.36	0.00	0.00	0.00	0.48	0.29	0.00	0
Na	0.03	0.04	0.01	0.04	0.68	0.66	0.00	0.03	0.00	0.53	0.70	0.07	0
K	0.77	0.79	0.88	0.85	0.00	0.00	0.00	0.81	0.00	0.01	0.01	0.48	0
Sum	7.68	7.67	7.72	7.73	5.02	5.03	1.99	7.72	2.00	5.02	5.00	6.69	29.48
Oxygen	11	11	11	11	8	8	3	11	3	8	8	11	46
X_{Mg}	0.54	0.60	0.45	0.54	–	–	0.01	0.53	0.01	–	–	0.54	0.18
X_{an}	–	–	–	–	0.32	0.35	–	–	–	0.47	0.29	–	–
Ti 22O	0.22	0.2	0.24	0.22	–	–	–	0.23	–	–	–	–	–

3.3. *Sample MD20–06*

Bulk rock major and trace element contents for sample MD20–06 are presented in Table 1 and Supplementary Material 1, respectively. The sample is less aluminous with respect to average metapelites (Fig. 3) and contains a markedly lower Al content and higher Mg and Ti content compared to MD21–02. Relative to MD20–05 and MD21–02, the bulk rock composition is strongly enriched in Cr (159–224 ppm) and V (306–360 ppm) but depleted in Zr (~170 ppm) and Sr (~50 ppm). Similarly, the bulk Nd and Sm are lower (~17 ppm and ~ 4 ppm, respectively).

MD20–06 contains very coarse, 2–3.5 cm-diameter, subhedral garnet (25–35 vol%) in a similarly coarse matrix of biotite (25–40 vol%), plagioclase (~10–13 vol%), quartz (~12–15 vol%), ilmenite (~6 vol%), and apatite. All regions of garnet contain abundant aligned inclusions of ilmenite and quartz that define a straight-to-sigmoidal internal fabric that is in places continuous with the external foliation (Fig. 4h); elsewhere, inclusions in the rims are steeply deflected into the external fabric at the outermost rim (Fig. 4f).

Phase analyses of MD20–06 are presented in Table 2 and Supplementary Material 2. In the matrix, multiple populations of biotite define the principal matrix foliation that is continuous with inclusions in garnet and an incipient overprinting secondary foliation (Fig. 4h), but these populations are compositionally indistinguishable (X_{Mg} ~ 0.55). Inclusions of biotite in garnet have X_{Mg} of 0.45 to 0.6. Garnet also contains inclusions of tourmaline, large apatite, feldspar (X_{An} 0.28–0.33), intergrown biotite and chlorite (that may be prograde, or which may represent staurolite breakdown), and a fine-grained replacement product (possibly after epidote or chloritoid). Small inclusions of white mica can also be found parallel to the internal foliation in garnets cores, and staurolite is sporadically present as rounded, near-rim inclusions. Neither white mica nor staurolite are found in the matrix. No aluminosilicates phases were observed in this sample.

Garnet chemical zoning

Garnet in MD20–06 displays concentric geochemical zoning, as exemplified by the bell-shaped spessartine pattern in Fig. 5c. Core compositions are ~7 mol% spessartine, ~6 mol% pyrope and ~ 14–15 mol% grossular whereas rims have ~15 mol% pyrope and ~ 9 mol% grossular. Almandine exhibits an m-shaped rim-to-rim profile, with the innermost core containing ~70 mol% almandine, mantle peaks of 73–74 mol%, and 70–71 mol% at the outer rim. Directly surrounding biotite inclusions, almandine and pyrope is steeply enriched and depleted, respectively, in regions approximately 75–100 μm wide (Fig. 5d).

LA-ICP-MS maps and trace element/REE plots reveal that despite diffuse REE zoning, garnets in MD20–06 contain narrow and steep high-MREE–HREE core that coincide with the compositional core defined by spessartine content (Fig. 7a, b, Supplementary Material 4). In the mantle of all grains, there are diffuse 300–400 μm-wide shoulders in MREE–HREE and Y that are concentric about the core and analogous to those documented in almandine (Figs. 5c and 7b). Narrow 50–100 μm zones at the outermost rims that are parallel to the present surface of the

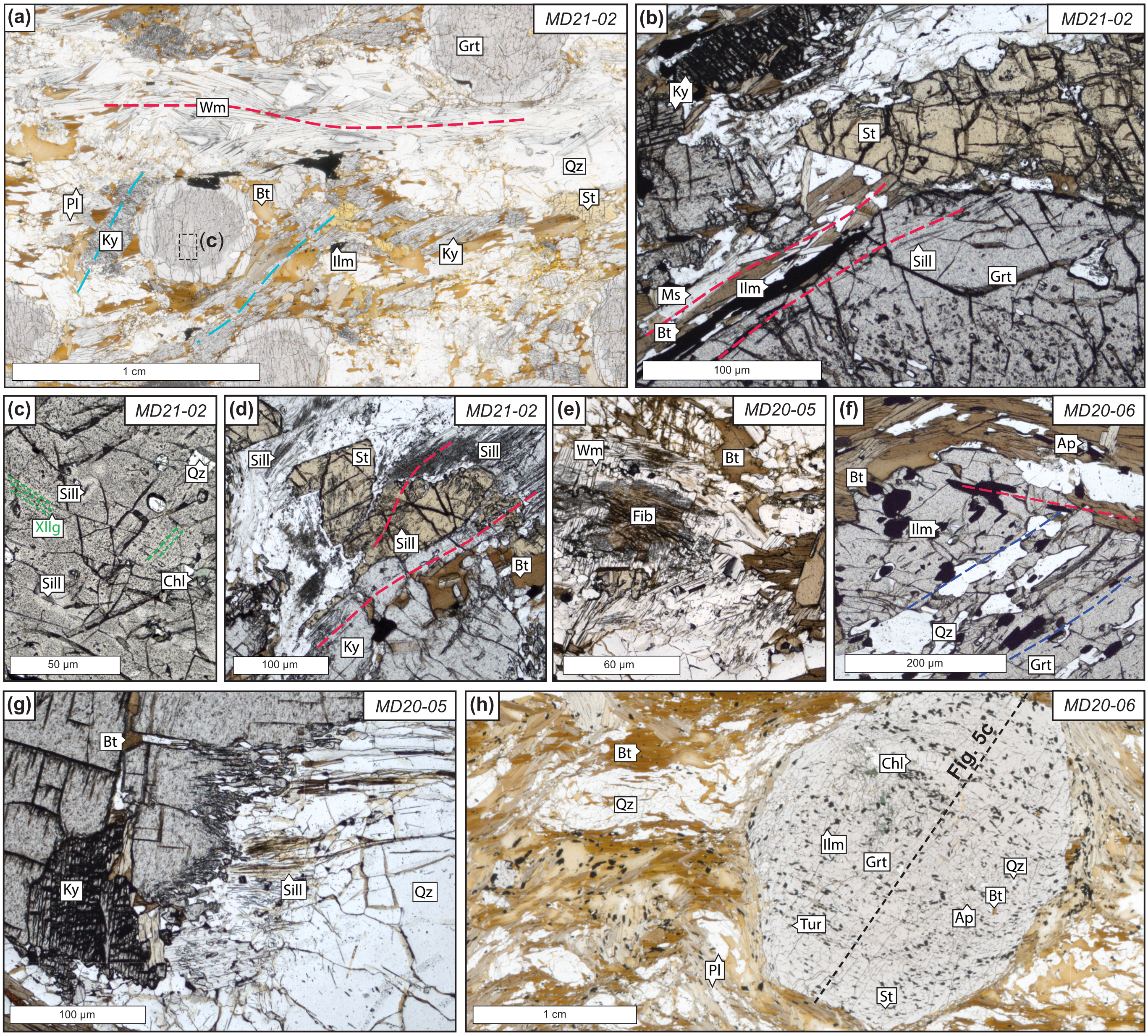

Fig. 4. Representative microstructures in Loch Raven Schist. All photomicrographs in plane-polarized light. (a) Typical microstructure of MD21–02. (b) Representative garnet rim in MD21–02 containing sillimanite inclusions aligned with external fabric. (c) Inclusions in the core of garnet from MD21–02 with primary inclusions of sillimanite, quartz and chlorite. Secondary, crystallographically-aligned inclusions are absent in the vicinity of sillimanite clots. (d) Inclusions of sillimanite in garnet and staurolite that are continuous with the external foliation. (e) Clots of fibrolite rimmed by white mica in MD20–05. (f) Garnet porphyroblast in MD20–06 showing truncation of internal foliation and reorientation of ilmenite and quartz inclusion in outermost rim of garnet, parallel to external foliation. (g) Kyanite in MD20–05 with ragged margins preserving incipient and aligned tranformation to sillimanite. Muscovite contains needles of sillimanite. (h) Typical microstructure of MD20–06; dashed line is transect in Fig. 5c.

garnets are enriched in Mn, Y, and MREE–HREE (Fig. 7a, Supplementary Material 4). The Cr zoning in garnet is not concentric (Supplementary Material 4) and exhibits none of the step changes documented in MD21–05 and MD20–05. The distribution of Sm and Nd in the garnets of MD20–06 is patchy, with little discernable core-to-rim zoning. Spot analyses of inclusion-free garnet indicate Sm and Nd concentrations are 0.4–1.2 ppm and 0.4–0.6 ppm, respectively (Fig. 7e).

4. Sm-Nd garnet geochronology

Sm–Nd garnet geochronology is a well-established and effective method to directly constrain the growth age of this key porphyroblastic metamorphic indicator mineral (e.g., Baxter et al., 2017). Preservation of primary major element and trace element zonation in all samples (see above) indicates that Sm–Nd garnet ages will record the timing of prograde to peak metamorphic heating (rather than subsequent diffusional resetting and closure). For the large garnets available in this study, core to rim age variations may also be extracted by selective picking and/or microdrilling and geochronologic analysis.

4.1. Analytical methodology

4.1.1. Extraction of core-to-rim garnet segments

A large volume (~30 × 10 × 10 cm) candidate sample of MD20–06 was initially segmented using parallel cuts with a ~ 0.75 cm spacing. These slabs were then cut and ground further to expose the largest

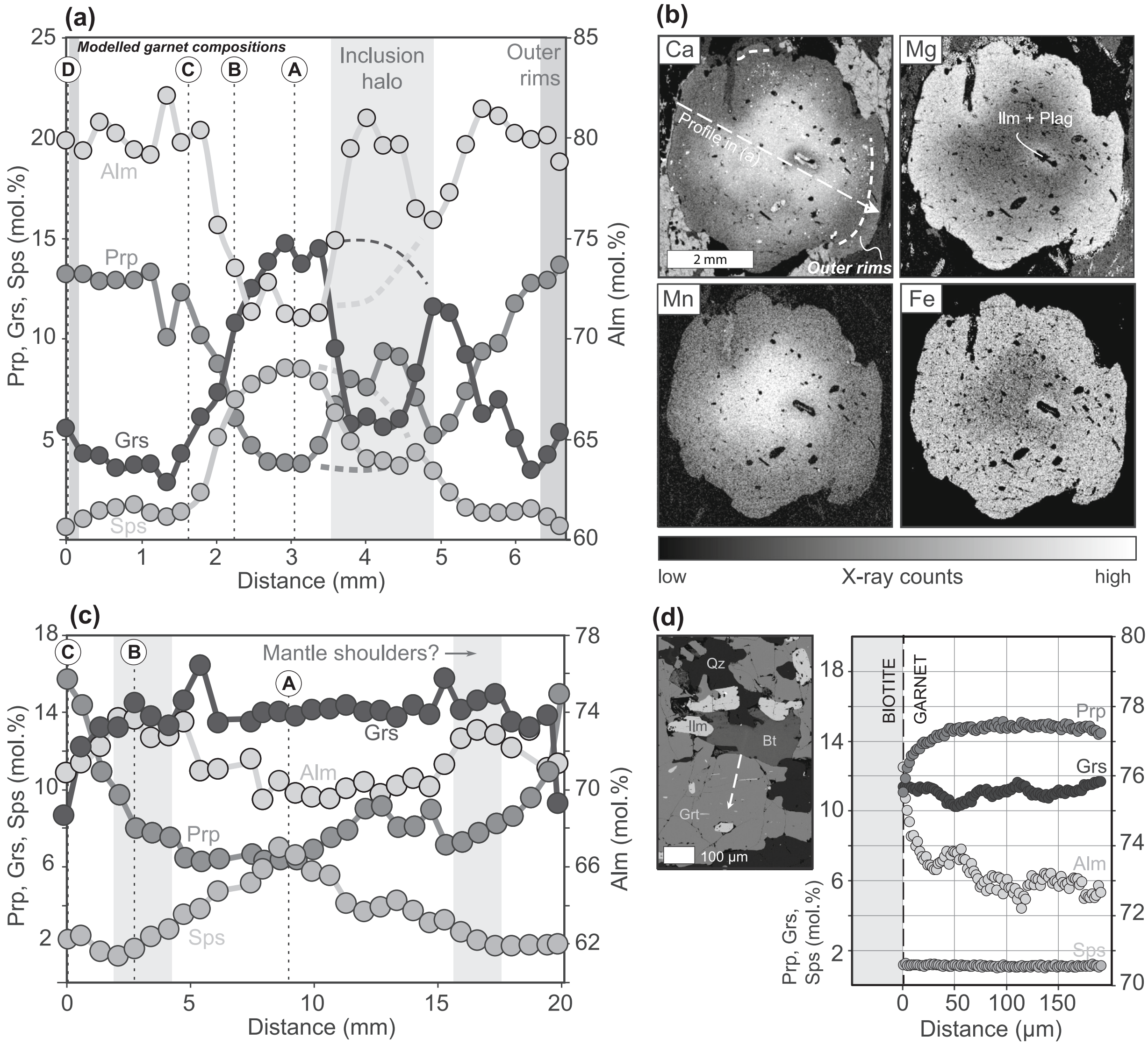

Fig. 5. Major element zoning of representative garnet. (a) Rim-to-rim transect across MD21–02 garnet. (b) Major element X-ray maps of garnet analyzed in (a). (c) Rim-to-rim transect across garnet in Fig. 4h, in MD20–06. (d) High-resolution transect in garnet in MD20–06, moving away from included biotite and imaged with backscatter electron imaging. In (a) and (c), circled letters denote compositions used for garnet fractionation modelling.

possible garnet surfaces, interpreted as best approaching a central section of garnet porphyroblasts. Once ground to 2.5 mm-thick, a 3 × 3 cm wafer was polished and the garnet imaged using the LA-ICP-MS raster mapping techniques described above. The LA-ICP-MS map of Mn concentration was used to guide microsampling of compositionally specific garnet segments using a New Wave MicroMill at the Center for Isotope Geochemistry, Boston College, following methods outlined in Pollington and Baxter (2011). The 2.5 mm-thick garnet wafer was glued using Crystalbond to a graphite block and drilled in water using a tapered diamond-encrusted bit to produce trenches parallel to compositional isopleths. This produced four garnet segments for MD20–06, labelled from S1-core to S4-rim (Fig. 7a). A matrix fraction (whole rock minus garnet) ~2.5 mm wide and directly adjacent to the drilled garnet was also extracted. After drilling, fractions were removed from the graphite block and sonicated in acetone to remove all Crystalbond.

Garnet crystals in fine-grained sample MD21–02 were too small to be drilled. Instead, crushed garnet was hand-picked to produce a glassy, clear pink fraction and a dusty, darker fraction. Based on thin section photomicrographs (Fig. 4a, b), these fractions are interpreted to approximate rim and core splits, respectively.

4.1.2. *Garnet purification and Sm–Nd garnet geochronology*

Subsequent separation of garnet fractions involved hand crushing, Frantz magnetic separation, and additional picking. Each separate (from both the bulk and drilled garnet fractions) was then hand-crushed using an agate mortar and pestle to grain sizes of 75–150 μm for chemical preparation; powder fractions (<75 μm) produced during this stage were retained for analysis and are labelled "Pwd" in the results. Representative whole rock fractions were selected and crushed to a powder in a ceramic ring mill. For MD20–06, the drilled matrix fraction was also hand-powdered.

Removal of micro-inclusions such as phosphates, which commonly contain order of magnitude higher concentrations of Sm and/or Nd, is key to producing accurate and precise Sm—Nd garnet dates. To remove these inclusions in both samples of this study, we used a 'partial dissolution method' (e.g., Harvey et al., 2021; Pollington and Baxter, 2011). First, aliquots of 58–96 mg of garnet and corresponding powder were chemically leached in 2 mL of 7 N nitric acid (HNO_3) for 2 h at 120 °C. Low concentration (2%–8%) hydrofluoric acid (HF) acid was then added to the decanted and dried garnet separates for two hours at 120 °C. The concentration of HF was modified based on the starting masses of separates to control the amount of dissolution. A subsequent stage with 2 h

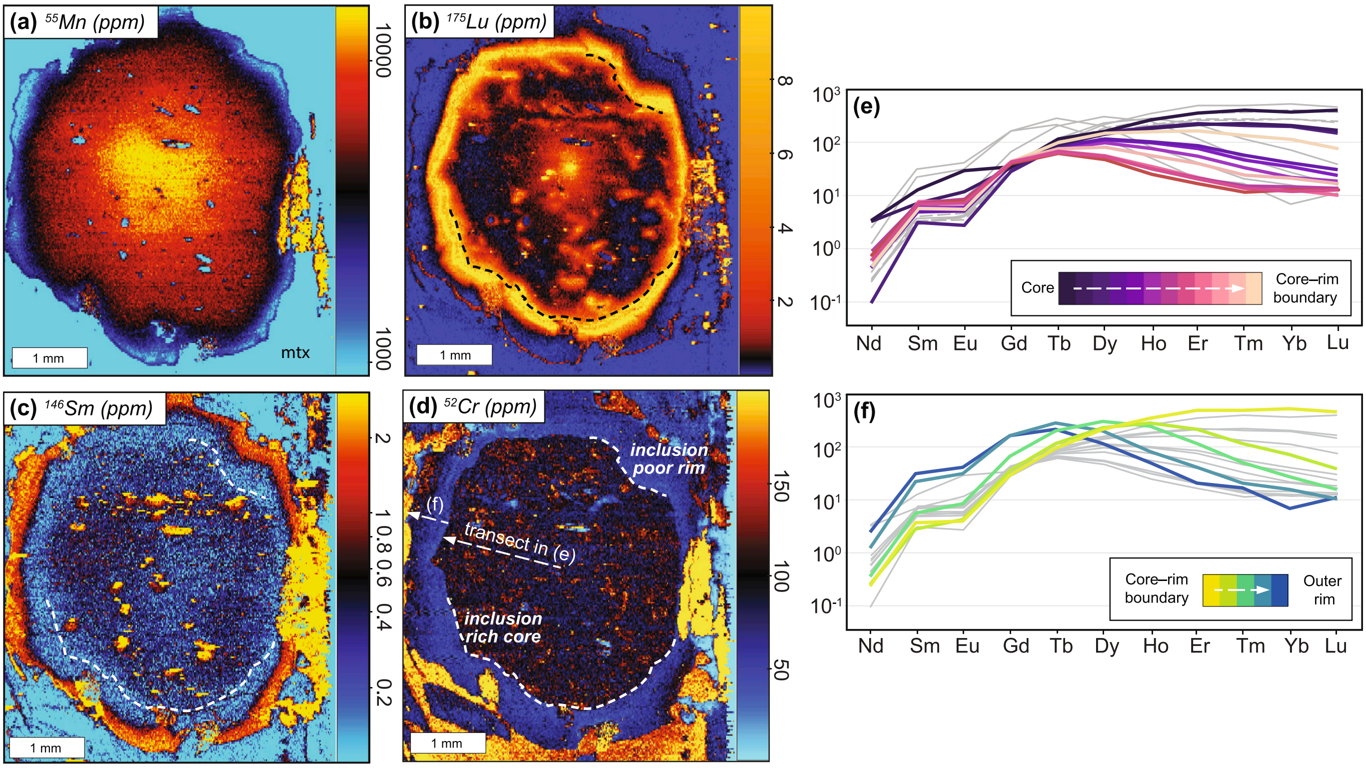

Fig. 6. Representative chemical zoning determined using LA-ICP-MS in garnet from MD20–05. (a) Mn concentration. (b) ^{175}Lu. (c) ^{146}Sm. (d) ^{52}Cr. (e) and (f) Chondrite-normalized (to McDonough & Sun, 1995) spider diagram derived from spots across inclusion-rich core (e) and inclusion-free rim (f) of garnet.

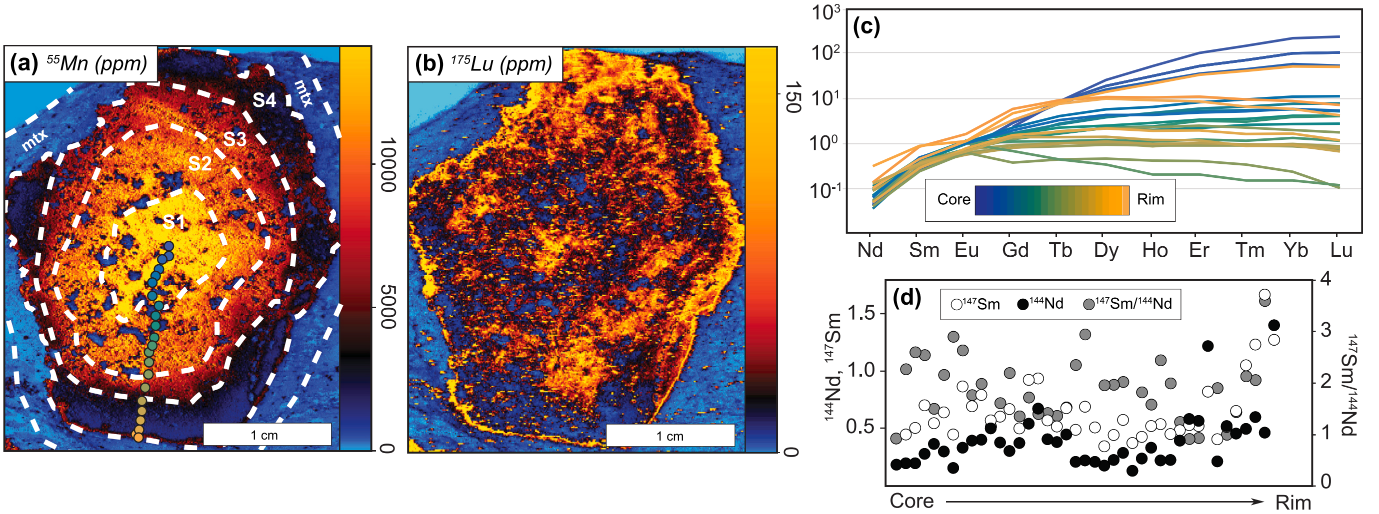

Fig. 7. Representative chemical zoning determined using LA-ICP-MS in two garnets from MD20–06. (a) Mn concentration with location and width of microdrilled trenches to isolate zones S1 to S4 and matrix ('mtx') fraction for Sm—Nd geochronology. (b) ^{175}Lu concentration. (c) Chondrite normalized (to McDonough & Sun, 1995) spider diagram for core-to-rim points illustrated in (a). (d) Sm and Nd concentrations determined by LA-ICP-MS along spot profile in (a).

of 7 N HNO_3 dissolution removed any secondary fluorides produced during preceding HF treatment. This two-stage HF + HNO_3 cycle was combined and repeated with varying concentrations of HF to progressively dissolve the garnet separate until the remaining garnet residue was reduced to 10%–40% of its original weight, whilst retaining sufficient material for analysis. The progressive combined HF and HNO_3 leachates (labelled L1, L2, etc.) were collected for analysis following Starr et al. (2020).

Following partial dissolution, all sample residues, garnet powders, and leaches were fully dissolved using a combination of HNO_3, HF and HCL. Whole rock and matrix powder fractions were also subject to complete dissolution using a combination of HNO_3, HF and HCL. After full dissolution, all samples and leaches were spiked with a well-calibrated mixed ^{147}Sm–^{150}Nd tracer prior to chemical separation by column chromatography (Harvey and Baxter, 2009). Cation exchange columns used AG50w-X4 resin and HCl to remove Fe and other divalent cations. Rare earth elements were isolated using Eichrom Tru-spec resin with HNO_3. Sm and Nd were then separated using AG50w-X4 resin and 2-methyl lactic acid. Three-column blanks were run simultaneously with the samples and spiked with 1–2 mg of the ^{147}Sm–^{150}Nd tracer prior to analysis.

Samples were analyzed in three sessions using an IsotopX Phoenix

Thermal Ionization Mass Spectrometer (TIMS) at the Boston College Centre for Isotope Geochemistry. For each sample, 0.9–257 ng of NdO was loaded onto rhenium filaments in a Ta_2O_5 activator slurry, and 3–59 ng Sm was loaded in HNO_3 onto tantalum filaments. Analyses of an in-house 4 ng NdO and 20 ng Sm standard (AMES metal) over the duration of analyses for this study yielded an external precision of $^{143}Nd/^{144}Nd = 0.512155 \pm 9$ ($n = 19$) and $^{147}Sm/^{152}Sm = 0.560869 \pm 41$ ($n = 11$) which are within the long term means of 0.512152 ± 11 ($n = 355$) and 0.560873 ± 45 ($n = 249$). External reproducibility of $^{147}Sm/^{144}Nd$ is 0.045% based on repeat analyses of a mixed gravimetric Sm–Nd normal solution.

4.2. Results

Data determined by TIMS are reported in Table 3. Overall, Sm concentrations in the cleanest garnet separates determined by TIMS and LA-ICP-MS are in good agreement: 0.8–1.4 ppm and 0.4–1.6 ppm, respectively. Similarly, Nd of equivalent fractions determined by TIMS are c. 0.2–0.3 ppm and LA-ICP-MS values are 0.2–0.68 ppm. This indicates success in removing problematic inclusions.

Multiple fractions of the MD21–02 whole rock powder (bulk alq1 and alq2) were analyzed. Concentrations from TIMS are c. 18 ppm Sm and c. 87 ppm Nd, similar to whole rock Sm and Nd concentrations determined in glasses, approximately 16 ppm and 76 ppm, respectively (Supplementary Material 1). For MD20–06, there is more discrepancy in the whole rock compositions. The whole rock MD20–06 aliquot (bulk alq1) analyzed by TIMS yields 19 ppm Sm and 101 ppm Nd, higher than measured in glass using LA-ICP-MS, 4 ppm Sm and 17 ppm Nd (Supplementary Material 1). However, the Mtx fraction determined using TIMS contains 5 ppm and 22 ppm Sm and Nd, respectively, equivalent to that determined externally in a bulk glass with LA-ICP-MS. This discrepancy may suggest that the powder created for the bulk compositional analyses was dominated by the matrix fraction, rather than oversampling garnet.

All but one (which has $^{147}Sm/^{144}Nd$ of 0.3) of the garnet, garnet powder, and leachate fractions have $^{147}Sm/^{144}Nd > 1$, suggesting that garnet fractions have been sufficiently cleansed of inclusions to determine an accurate garnet age (Baxter et al., 2017). Whole rock $^{147}Sm/^{144}Nd$ are 0.122 for MD21–02 and 0.114 for MD20–06, and the matrix immediately in the vicinity of the garnet rim in MD20–06 has $^{147}Sm/^{144}Nd$ if 0.136. Using these data, Sm–Nd isochrons were constructed using IsoplotR (Vermeesch, 2018); and the preferred ages are shown in bold on Fig. 8 and reported in Table 3.

In isochron age error propagation the poorer (higher) of the internal run precision or the external precision based on the long-term reproducibility of the in-house AMES metal standard was used to determine the uncertainty. Ages and uncertainties are determined with the IsoplotR software and are reported as either as 2σ or as 2σ times the square root of the MSWD for samples with elevated MSWDs (Vermeesch, 2018). This modification of the uncertainty requires the assumption that all analytical uncertainties have been underestimated by this factor. While this is likely not a valid assumption (cf. Harvey et al., 2021), the inflated uncertainties are viewed as reasonable estimates of the uncertainty in the isochron-derived age. Several initial aliquoted separates of MD20–06 ($S1_2$ alq1 and $S4_4$ alq1) had high Pr interferences ($^{141}Pr/^{144}Nd > 3.5$) rendering them of questionable accuracy; these data are not included in the reported isochron ages but have similar Sm and Nd concentrations to repeat analyses (i.e., $S1_2$ alq2 and $S4_4$ alq2) so are included in Table 3.

The preferred ages for the core and rim of MD21–02 are 391.5 ± 0.8 Ma and 383.1 ± 1.0 Ma (Fig. 8), with MDWDs of 0.8 and 3.7, respectively. For the coarse drilled garnet in MD20–06, results are dependent on whether the WR alq1 (i.e., bulk powder) or the Mtx (i.e., the c. 2.5 mm of adjacent matrix) is used. If the bulk powder is used, the innermost core is 440.2 ± 8.3 Ma. Moving rimward, subsequent fractions are 439.2 ± 8.5 Ma, 436.1 ± 5.1 Ma, and 433.9 ± 3.7 Ma. These data yield high MSWDs of 11–30. In contrast to overdispersion when using WR as a low Sm/Nd point, assuming isotopic equilibration only with the adjacent matrix leads to relative underdispersal (MSWDs of 0.1–3.7) and non-progressive garnet ages from core-to-rim: 416.6 ± 2.6 Ma, 423.0 ± 1.6 Ma, 425.4 ± 1.1 Ma, and 423.9 ± 1.1 Ma. When both the WR alq1 and Mtx are included in isochron calculations, all dates cluster around 430 Ma, with large uncertainties (± 11–29 Ma) and MSWDs (160).

While it is possible to pair isotope ratios of individual garnet

Table 3
Sm–Nd isotopic data for garnet separates, drilled garnet zones, and matrix and whole rock separates.

	Nd loaded (ng)	Nd (ppm)	Sm (ppm)	$^{147}Sm/^{144}Nd$	±2 S.E.	$^{143}Nd/^{144}Nd$	±2 S.E.	$^{143}Nd/^{144}Nd$ (ppm 2 S.E.)
MD21–02								
WR alq2	19.8	87.534	17.701	0.12232	0.00007	0.512168	0.000011	11.12
Rim fraction								
Grt1	4.9	0.240	1.446	3.63659	0.00196	0.520951	0.000012	14.44
Grt2	3.8	0.192	1.525	4.81280	0.00260	0.523905	0.000012	16.90
Grt2 Lch3	2.1	0.591	1.369	1.39626	0.00075	0.515335	0.000013	26.13
Core fraction								
Grt1	4.6	0.233	0.782	2.03398	0.00110	0.517062	0.000012	23.42
Grt2	2.6	0.174	0.777	2.70807	0.00146	0.518774	0.000012	20.51
Grt1 L3	12.4	2.232	1.092	0.29596	0.00016	0.512607	0.000005	10.15
Grt1 L4	0.8	0.249	0.918	2.23326	0.00121	0.517563	0.000033	63.89
MD20–06								
WR alq 1	209	101.41	19.176	0.11438	0.00006	0.512133	0.000011	5.91
Mtx	37.0	22.049	4.945	0.13565	0.00007	0.512332	0.000011	9.86
Drilled garnet segments								
$GrtS1_2$ alq1*	5.7	0.690	1.370	1.19804	0.00065	0.515240	0.000024	46.32
$GrtS1_2$ alq2	3.1	0.694	1.379	1.20237	0.00065	0.515208	0.000036	69.34
$GrtS1_2$ L4	5.0	1.474	2.450	1.00584	0.00054	0.514704	0.000011	13.60
$GrtS2_1$ alq1	4.6	0.692	1.888	1.65089	0.00089	0.516527	0.000012	18.30
$GrtS2_2$ L4	4.5	0.884	1.846	1.26332	0.00068	0.515459	0.000011	11.29
$GrtS3_1$ alq1	4.9	0.580	2.197	2.29132	0.00124	0.518322	0.000012	17.35
$GrtS3_1$ L4	2.6	0.772	2.246	1.75858	0.00095	0.516844	0.000012	22.93
$GrtS4_2$ alq1*	5.2	0.711	2.683	2.28399	0.00123	0.518312	0.000022	43.34
$GrtS4_2$ alq2	4.2	1.063	4.122	2.34510	0.00127	0.518444	0.000012	13.20
$GrtS4_2$ L4	3.3	0.526	1.836	2.11243	0.00114	0.517818	0.000014	26.76

Note. Grt, garnet; Pwd, powder; L, leachate; WR, whole rock powder; alq, aliquot.

* Excluded from isochron (see discussion).

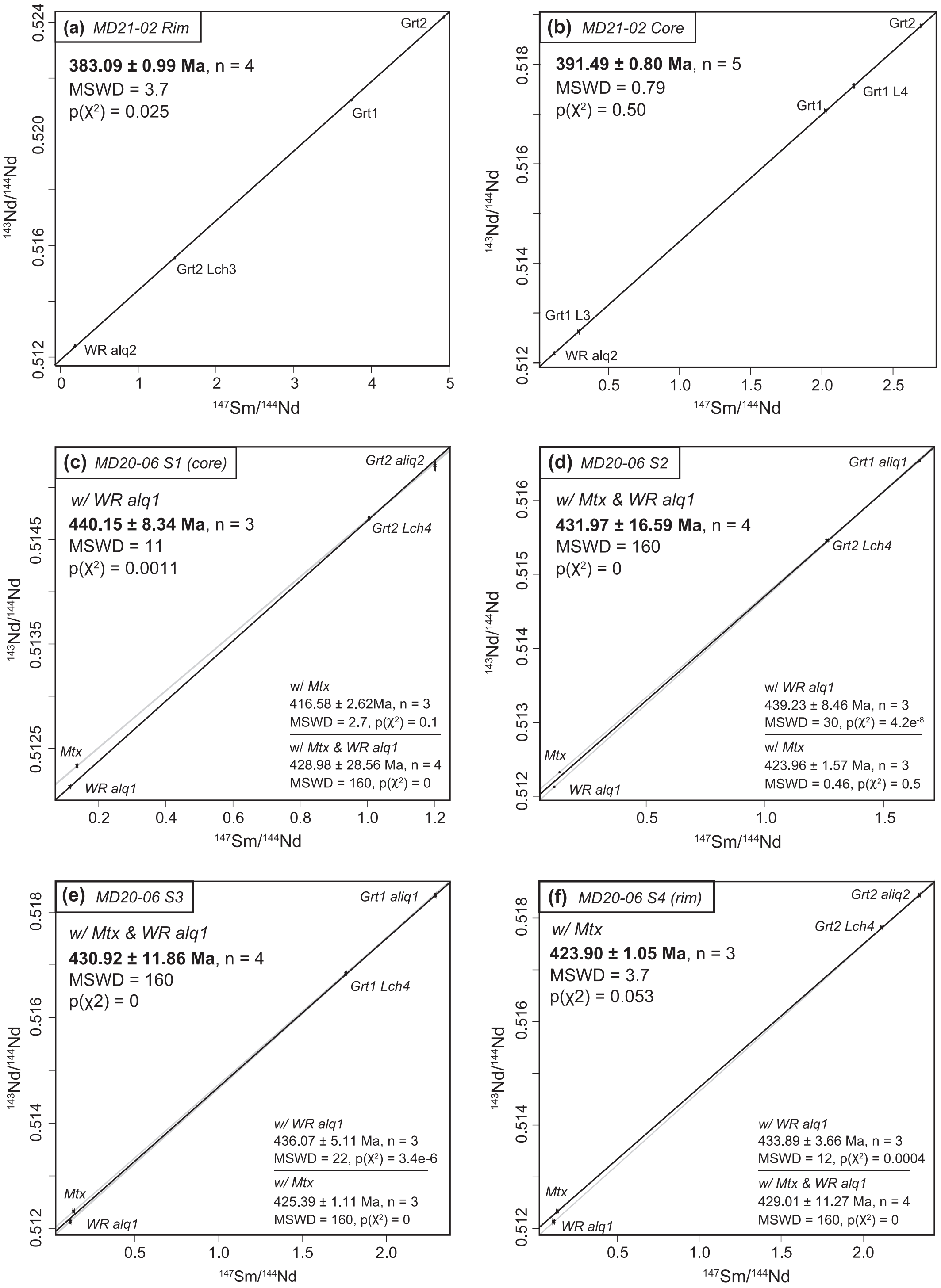

Fig. 8. Garnet-whole rock/matrix powder Sm–Nd isochrons for (a) the rim split of MD21–02, (b) the core split of MD21–02, and (c)–(f) four drilled core-to-rim garnet segments from MD20–06. The final reported age uncertainty is either 2σ confidence or 2σ times the square root of the MSWD for samples with high MSWDs (5.3–79, chi-squared *p*-value <0.02). The preferred age for each sample is in bold, plotted with a solid black isochron.

segments with individual matrix and/or whole-rock isotopic compositions to construct two-point isochrons, cm-scale matrix heterogeneity and whole-rock isotopic compositions suggest that garnet segments may have equilibrated with locally distinct matrix isotopic compositions, as discussed by Gatewood et al. (2015). The coarse size of the garnets in MD20–06 (2–3.5 cm diameter) may have precluded progressive re-equilibration of the interior of garnet with the fractionating matrix for much of the duration of garnet growth. Only very incipient stages of growth may have occurred in equilibrium with the bulk rock composition (i.e., WR), and the latest growth of garnet occurring in equilibrium with the most fractionated remaining matrix (i.e., Mtx).

It is therefore reasonable to pair the isolated core (S1) fraction with the WR aliquot, and the rim fraction with the directly adjacent matrix with which the garnet exhibits microstructural continuity. In this case, the 440.2 ± 8.3 Ma core age (S1) and 423.9 ± 1.1 Ma rim age (S4) yield a total growth duration of 16.3 ± 8.4 Myr. These are preferred ages for core and rim and the timespan between them. Mantle fractions S2 and S3 fall within this range. However, lengthscales for garnet-rock isotopic equilibrium likely changed as individual garnets grew and incorporated atoms from larger rock volumes where cm-scale heterogeneity comes into play. Thus, garnet segments S2 and S3 must be fit (rather unsatisfactorily) to both the WR and Mtx (432.0 ± 16.6 Ma and 430.9 ± 11.9 Ma) yielding high MSWD and poor age precision reflecting the uncertainty in the evolving equilibrating matrix volume.

5. Thermobarometry

5.1. Methods

5.1.1. Phase equilibria modelling

To provide a framework for mineral growth in this study, phase equilibria were calculated using the Gibbs energy minimization software Theriak/Domino (de Capitani and Petrakakis, 2010). Modelling was performed in the 11-component system $MnO–Na_2O–CaO–K_2O–FeO–MgO–Al_2O_3–SiO_2–CO_2–H_2O–TiO_2$ using the internally consistent thermodynamic dataset ds-62 of Holland and Powell (2011; updated April 2021) and activity–composition relations for: garnet, biotite, cordierite, chlorite, chloritoid, staurolite, white mica, ilmenite and melt (White et al., 2014); magnetite (White et al., 2000); epidote (Holland and Powell, 2011); plagioclase (Holland and Powell, 2003).

To investigate uncertainty associated with differences in thermodynamic datasets and solid solution models, dataset ds-55 (Holland and Powell, 1998) was also tested. The more recent thermodynamic dataset ds-62 was ultimately chosen because it better predicted the observed mineral assemblages and the stability and composition of garnet in these samples. Uncertainty on the absolute position of the phase assemblage boundaries in P–T space generally are within ± 20–30 °C and ± 0.5 kbar at 1 s.d. (Palin et al., 2016; Powell and Holland, 2008), and results are used as a general guide rather than as absolute constraints.

5.1.2. Bulk compositions for modelling

An initial bulk rock composition for petrological modelling of MD21–02 was constructed by combining the average compositions of phases interpreted to represent peak pressure conditions (garnet, kyanite, muscovite, biotite, plagioclase, quartz, ilmenite), with point-counted modal abundances modified to account for pre- and post-peak assemblages. This targeted approach has been shown to be effective at modelling equilibration across the thin-section length scales from which our compositional analyses were obtained (e.g., Palin et al., 2016). For completeness, all modelling was also performed using the XRF-derived bulk; the position of univariant curves is very similar in both sets of models, and overall results are the same.

In MD21–02, H_2O is initially included in excess as a saturating phase, with activity of H_2O set to 1. However, given the evidence of early sillimanite growth in the form of unoriented inclusions in the core of garnet in MD21–02, the sample is interpreted to have undergone relatively high-T recrystallization prior to metamorphism associated with matrix garnet and kyanite/sillimanite. In the absence of intervening rehydration, this early sillimanite growth (via the breakdown of chlorite and white mica) would have dehydrated the bulk of MD21–02, such that it was potentially undersaturated at the onset of renewed (Devonian) metamorphism. Therefore, the H_2O contents of the present matrix–porphyroblastic assemblage are also explored by investigating where in MH_2O–T space the observed garnet core compositions are effectively reproduced by the model. For MD21–02, the bulk rock $X\mathrm{Fe}^{3+} = \mathrm{Fe}^{3+}/\mathrm{Fe_T}$ was taken as a function of the Fe^{3+} determined for all ferric minerals by stoichiometric charge balance. This value ($X\mathrm{Fe}^{3+} = 0.15$) is slightly lower than that determined using titration of the XRF powder ($X\mathrm{Fe}^{3+} = 0.25$).

Progressive fractionation of components into newly grown garnet in MD21–02 is also modelled by removing 100% of the composition of garnet from the incipient undersaturated bulk at 1 °C increments along simulated P–T paths (e.g., Baxter and Caddick, 2013; George and Gaidies, 2017). Garnet compositions used for comparison to models in a four-part fractionation sequence are denoted in Fig. 5a. The change in trace element concentration in garnet from inclusion-rich cores to inclusion-poor rims is not associated with a change in major element composition (Fig. 6), so no associated shift in prograde bulk composition was simulated.

For sample MD20–06, whole rock XRF data were used to approximate the initial bulk composition, with a proportional adjustment to total CaO to correct for the contribution made by apatite ($CaPO_4$) to the CaO total by assuming that all P_2O_5 resided in apatite. Given the abundance of coarse apatite in MD20–06 (~1 vol%), this is considered a reasonable approximation. Whole rock $X\mathrm{Fe}^{3+}$ of MD20–06 content was determined by titration. Initially, H_2O with $aH_2O = 1$ was included in excess. To account for dehydration along the prograde path, T–$M(H_2O)$ phase diagrams were also considered and are discussed below. As described for MD21–02, garnet stabilized along simulated 1 °C increment P-T paths in MD20–06 was 100% fractionated from the bulk composition. Garnet compositions used for the three-part fractionation series are denoted in Fig. 5c.

5.1.3. Independent thermobarometers

The Ti content of biotite (Henry et al., 2005) was used as an independent check on peak temperature. This geothermometer was calibrated for graphitic metapelites that contain ilmenite (or rutile) as a Ti-saturating phase, so is ideally suited to this study. Garnet–biotite thermometry (Holdaway, 2000) was also applied to discern potential differences between temperatures preserved by inclusions in garnet and at rims of garnet (Fig. 5d). Compositional data used for these calculations are given in Table 2, and results are summarized in Figs. 9 and 10.

In addition to these independent thermometers, the average P (av$P$) function in THERMOCALC (version tc340i) was applied. This approach performs least-squares regression on a set of independent end-member reactions. For consistency with Theriak/Domino modelling presented in the main portion of this work, end-member activities were calculated using AX6.2 (Holland, 2018) and phase compositions were interpreted to be associated with either (a) peak metamorphic conditions, or (b) incipient garnet growth.

5.2. Results

5.2.1. MD21–02

Fig. 9 presents calculated equilibria for MD21–02. In the case of an H_2O oversaturated bulk (Fig. 9a), isopleths of the observed garnet core compositions approach intersection at 4–5 kbar. Therefore, the degree of H_2O (under)saturation at incipient garnet growth was investigated at 4.5 kbar (Fig. 9b).

Fig. 9b and c indicate that isopleths of the grossular, pyrope and almandine contents of the earliest grown (core) garnet can be most effectively reproduced at bulk H_2O of 10.5–13.5 mol%, temperatures of 490–510 °C, and pressures of 4.4–4.9 kbar (point A). For this earliest recorded phase of garnet growth, av$P$ calculated using the compositions of inclusions in garnet and adjacent garnet confirms the approximate position of the core isopleth intersection at 500 °C, 4.3 ± 0.8 kbar (Fig. 9c). This is >50 °C above the first predicted equilibrium stability of garnet-bearing assemblages; such a discrepancy may be a consequence of enhanced garnet stabilization in undersaturated assemblages, related to overstepping of the garnet-in reaction, and/or inadequate sampling of the narrow compositional core of garnet in the analyzed thin section.

Using the same bulk rock composition, garnet mantle compositions intersect at c. 568 °C and 5.4 kbar (point B, Fig. 9c). Along a P–T trajectory from the core to these conditions, excess H_2O becomes a part of the stable assemblage at c. 560 °C and 5.3 kbar, derived from internal rehydration of the initially undersaturated bulk during prograde mineral growth. Using a bulk derived by fractionating all garnet stabilized up to point B, the next mantle increment could intersect at either c. 633 °C and 6.6 kbar (point C1, Fig. 9d) or 633 °C and 7.1 kbar (point C2, Fig. 9d). The former (C1) is in a divariant field in which garnet, plagioclase,

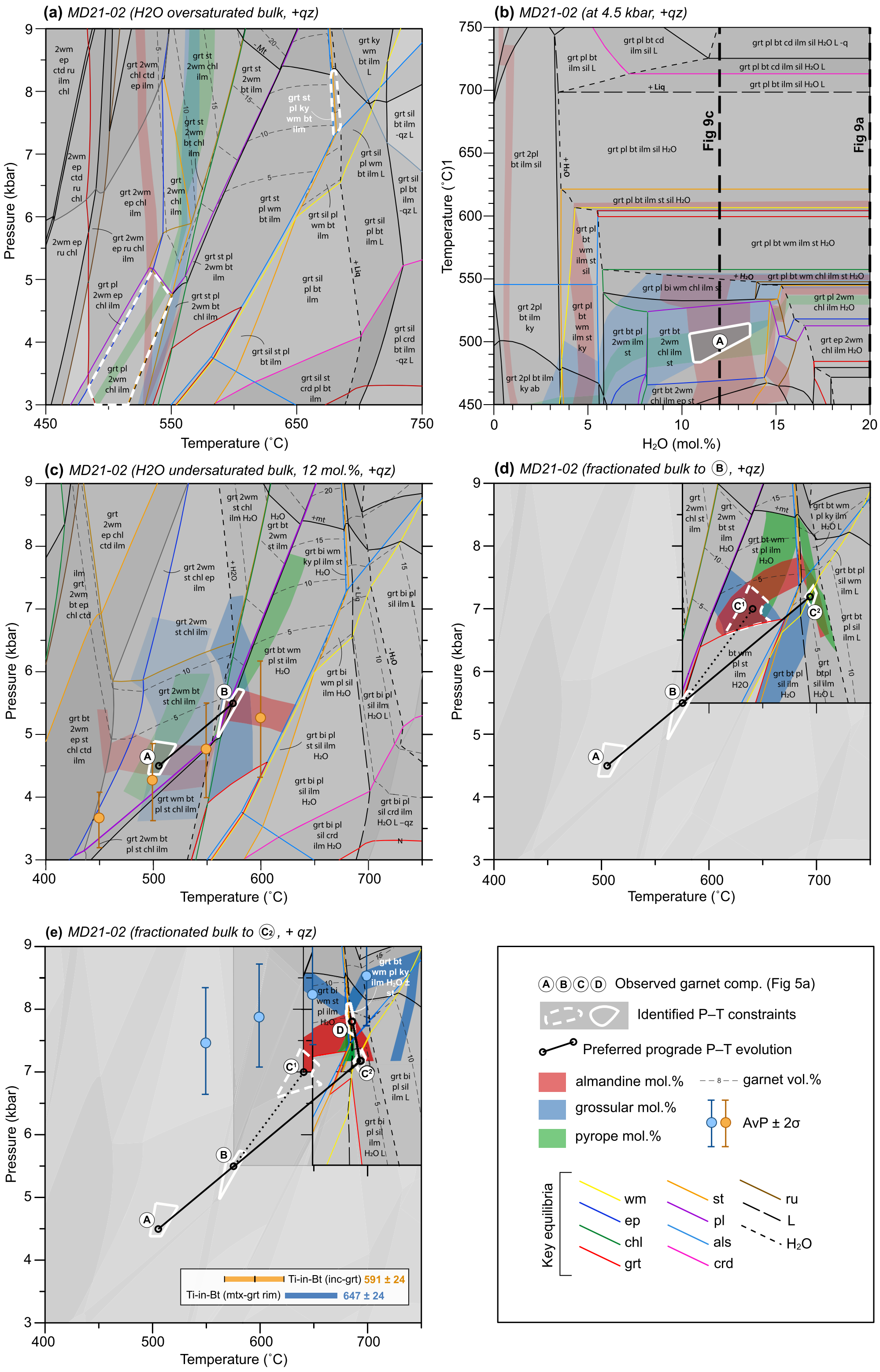

Fig. 9. Thermobarometric modelling of MD21–02. (a) Calculated *P*–*T* phase equilibria at H_2O oversaturated conditions. (b) *T*–*M*H_2O calculated at 4.5 kbar. (c) Equilibria at H_2O undersaturated conditions (12 mol% H_2O). Core isopleth intersection (A), mantle isopleth intersection (B), and results of Av*P* for core compositions (± 2 s.d.) shown. (d) Equilibria for fractionated bulk composition from (B) with two potential isopleth intersection locations for composition (C1 and C2). (e) Equilibria for fractionated bulk composition from C, with peak-*P* metamorphic assemblage highlighted in bold. Results of Av*P* for rim and matrix compositions (± 2 s. d.), and results of Ti-in-biotite thermometer included. Solid black lines denote preferred metamorphic history.

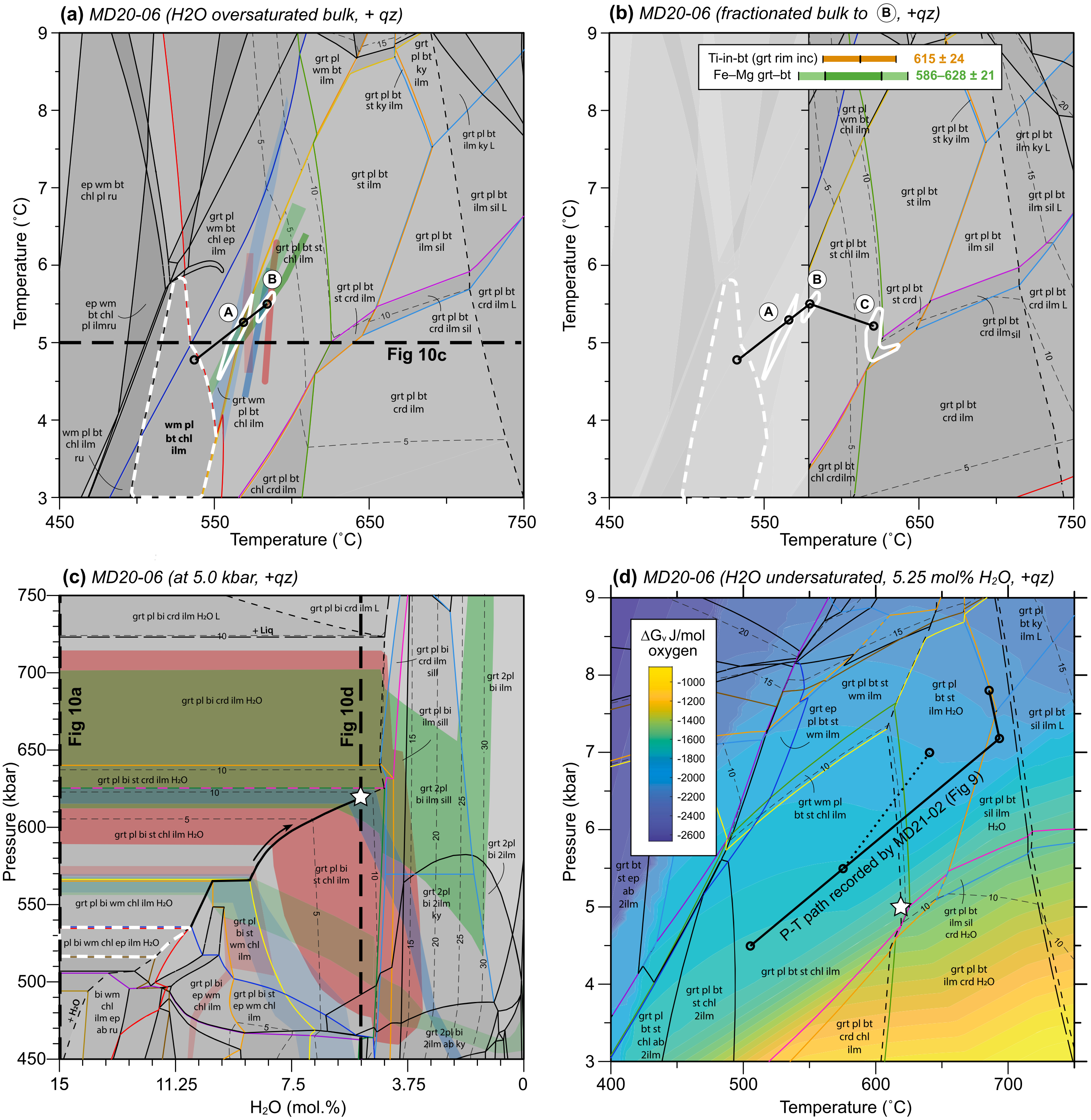

Fig. 10. Thermobarometric modelling of MD20–06. (a) Calculated *P*–*T* phase equilibria at H_2O oversaturated conditions, with isopleth intersection using compositions from Fig. 5c in white polygons. (b) Equilibria for fractionated bulk composition from (B), contoured for isopleths of observed garnet rim compositions. Results of Ti-in-biotite and Fe—Mg garnet-biotite thermometry shown. (c) *T*–*M*H_2O, calculated at 5 kbar. (d) Equilibria at 5.25 mol% bulk H_2O contoured according to the driving force for garnet nucleation (ΔG_v in J/mol of oxygen). White stars in (c) and (d) denotes the dehydrated peak metamorphic conditions. Legend as in Fig. 9.

staurolite, biotite, white mica, and ilmenite are stable. In the latter (C2), garnet, sillimanite, biotite, plagioclase and ilmenite are stabilized, and white mica and staurolite are destabilized. Along both trajectories, constrained conditions are preceded by a *P*–*T* interval in which garnet is not a part of the stable assemblage (Fig. 9d). While both trajectories (B to C1 or C2) are plausible, evolution along a higher geothermal gradient (C2) stabilizes pre-peak *P* sillimanite at a position between compositions B and C in garnet (Fig. 5), consistent with the observation of aligned foliation-aligned sillimanite inclusions in the outer rims of garnet. Observations of staurolite with decomposing textures in MD21–02 are consistent with an appreciable period in which staurolite is not stable. We therefore consider this *P*–*T* trajectory the most plausible. Results of Ti-in-biotite thermometry using biotite included in the mantle regions of garnet, yield a population at 591 ± 24 °C (Fig. 9e); these temperatures are consistent with (partial) equilibration having occurred along this prograde path.

After final fractionation of garnet at 683 °C and 7.1 kbar (C2), kyanite is part of the stable assemblage at $P > 7.4$ kbar and $T > 680$ °C, close to the H_2O-saturated solidus at $T = 685$ °C (Fig. 9e). Given the absence of evidence for anatexis in this sample, the observed peak

Table 4
Data summary. Sm—Nd garnet ages are the preferred age for each sample (see text for additional details).

Sample	Preferred Sm– garnet age	Grt diameter (mm)	Grt vol %	Matrix assemblage	Garnet inclusion assemblage
MD21–02 rim	383.1 ± 1.0	2–5	13–22	Wm + Bt + Qz + Pl + St + Ky + Sil + And + Ilm + Tur + Ap + Zrc + Mnz	Qz + Sill + Wm + Ap + Bt + Ilm + F.I. Sil + Ilm
MD21–02 core	391.5 ± 0.8				
MD20–06 S1 (core)	440.2 ± 8.3	20–35	25–35	Bt + Qz + Pl + Ilm + Ap + Zrc + Mnz	Qz + Ilm + Bt + Ap + Tur + Wm ± St
MD20–06 S2	431.97 ± 16.6				
MD20–06 S3	430.9 ± 11.9				
MD20–06 S4 (rim)	423.9 ± 1.1				

assemblage containing stable or metastable staurolite is considered to be closely associated with these constraints. Therefore, peak pressure conditions are inferred to have occurred within a relatively small P–T range, at 680–700 °C and 7.5–8.5 kbar. Here, calculated isopleths of almandine, grossular, and pyrope are in the range of the measured garnet rim compositions (Fig. 5a), and garnet abundance is 10–20 vol%. The predicted modal abundances of plagioclase and quartz (30–35 vol %), muscovite (16–20 vol%), ilmenite (~3 vol%), biotite (15–20 vol%), and aluminosilicate (~5–8 vol%), recalculated in the absence of a melt component are all directly comparable to those observed in MD21–02 (cf. Section 3.2). This preferred P–T trajectory and modal constraints is nearly equivalent to that which would be determined using a H_2O oversaturated bulk composition and unfractionated garnet core and rim isopleths (dashed polygons, Fig. 9a).

Assuming equilibration of garnet rims and matrix biotite, Ti-in-biotite thermobarometry of 647 ± 24 °C yield peak metamorphic temperatures that are slightly lower than those determined using phase equilibria. However, AvP calculations performed assuming equilibration between garnet rims and matrix phases yield pressures comparable to conditions at which kyanite becomes part of the stable assemblage, at 7–9 kbar at 600–750 °C. For a 50 °C step size, AvP uncertainties are minimized between 650 °C and 700 °C, where $P = 8.2$ kbar and 8.5 kbar, respectively.

In thin section, textures at the interface of matrix sillimanite and kyanite (Fig. 4f) are suggestive of direct replacement of the kyanite by sillimanite. Less than 1 kbar of post-peak decompression from peak-P would re-stabilize sillimanite-bearing assemblages and can therefore account for this observation (Fig. 9a, e).

5.2.2. MD20–06

Unlike in MD21–02, sample MD20–06 contains no evidence for a dehydrated precursor assemblage (early sillimanite growth), so initial calculated equilibria utilize a H_2O-oversaturated bulk composition (Fig. 10a). The predicted P–T conditions of the observed inclusion assemblage in garnet is 500–540 °C and < 4–5.5 kbar (black dashed field, Fig. 10a). Starting with these approximate conditions, constraints on the prograde path can be placed. Above the garnet-in, calculated isopleths of the measured core pyrope, almandine, and grossular content intersect in a region at ~550 °C and c. 4.8–5.5 kbar (point A, Fig. 10a). Along a fractionating P–T path from below the garnet-in and through this intersection, staurolite is stabilized and white mica is destabilized at ~570 °C, before mantle compositions are reproduced at ~580 °C and ~5.5 kbar (point B Fig. 10a). This is consistent with observed inclusions of muscovite and staurolite in garnet cores, and the absence of muscovite in the matrix.

Using a bulk composition obtained by fractionating garnet to point B, a slight prograde drop in pressure to 4.7–5.4 kbar and an increase in temperature to 620–630 °C reproduces garnet rim compositions (point C of Fig. 10b). At these conditions, cordierite is not stabilized at high T, but staurolite and chlorite remains a minor part (<3 vol% and 0.1 vol%, respectively) of the assemblage. Neither cordierite, staurolite, or prograde chlorite is present in thin section. Uncertainty associated with the calculated positions of the univariant curves or a slight increase in peak T to 640–650 °C (where core isopleths also intersect and staurolite and chlorite is destabilized) and overstepping of cordierite crystallization may account for these discrepancies. Alternatively, cordierite may have been a part of the stable peak assemblage at slightly higher T; though not observed in MD20–06, clots of biotite may be retrograde after chloritoid, similar to intergrowths of biotite and an Al_2SiO_5 polymorph documented by Bosbyshell et al. (2005) and interpreted to have replaced cordierite in the Wissahickon Schist.

Taken together, these constraints suggest sample MD20–06 may have evolved along an near-isobaric path, at ~4.5–5.5 kbar to a maximum T of ~625 °C. Results of Ti-in-biotite thermometry using matrix compositions (615 ± 24 °C) are within error of this estimated peak temperature, but av$P$ was unable to converge on a solution. Fe—Mg garnet–biotite exchange thermometry, applied to inclusions distributed across mantle to rim regions of garnet yield temperatures of 586–628 °C, potentially reflective of progressive entrapment temperatures. Given the low-Al bulk rock composition and the resulting reduced low-P stabilization of aluminosilicates (no andalusite stability and sillimanite only becoming stable at $P > 5$–5.5 kbar), this approximate thermal history is considered reasonable. Moreover, almandine content (Fig. 5c) displays pronounced M-shaped zoning that often typifies zoning in garnet grown at relatively low and homogeneous pressures.

To assess the influence of H_2O content on the stability of metamorphic assemblages in MD20–06, a T–$M(H_2O)$ plot was constructed at $P = 5$ kbar. Because fractionation of garnet does little to modify the overall topology (compare Fig. 10a and b), the composition is fixed to the initial bulk. At 5 kbar, >15 mol% bulk H_2O is needed to saturate all assemblages at temperatures exceeding 450 °C. As temperature increases to c. 625 °C, H_2O saturation is achieved at progressively lower $M(H_2O)$, related to the up-T loss of hydrous phases. Between 625 °C and 725 °C, only ~4.5 mol% H_2O is required for saturation.

The observed inclusion assemblage in garnet (white mica, plagioclase, biotite, ilmenite, chlorite, quartz, with or without altered epidote) is principally stable in the H_2O oversaturated domain. Heating at c. 5 kbar in a system closed to the loss of internally derived fluids is approximately equivalent to the P–T trajectory discerned using garnet compositions in Fig. 10b. However, if excess fluid (not crystallographic bound) is allowed to drain from the system along the prograde path, the $M(H_2O)$ along the P–T path in Fig. 10b would be expected to evolve along the H_2O saturation curve in Fig. 10c. In this open-system scenario, minimum saturation of ~5.25 mol% H_2O of would be reached at ~620 °C, conditions where garnet rim compositions can be effectively reproduced (white star, Fig. 10c). Along this dehydration trajectory, H_2O in solid phases evolves from ~3.5 wt% to 1.5 wt%.

Excluding the aforementioned prediction of staurolite and chlorite stability, at these peak P–T–$M(H_2O)$ conditions the predicted matrix mineral modes of are comparable to those observed, including biotite (maximum 37 vol% modelled versus 35 vol%), plagioclase (19 vol% versus 13 vol%), ilmenite (6 vol% versus 4 vol%), and quartz (24 vol% versus maximum 15 vol%) quartz. However, modelled garnet abundance in any region of the H_2O-saturated domain does not exceed ~10 vol% (Fig. 9c). This relative paucity of modelled garnet is in pronounced contrast to the observed abundances in MD20–06 (Table 4), and increases the relative abundance of other modelled phases. These low garnet modes in our models may related to the discrepancy between the

Sm—Nd content measured in glass and in the whole rock aliquot during TIMS analyses; the common fraction used for XRF and LA-ICP-MS analyses may have under-sampled garnet relative to the matrix contribution. Moreover, as discussed by Palin et al. (2016), modal estimates of porphyroblastic schists (even coupling both thin sections and hand specimens) are particularly subject to inaccuracies relating to extrapolation from 2D slices to 3D rock volumes. Therefore, discrepancies in modelled versus observed modes in MD20–06 are not interpreted as significant.

Interestingly, at 5 kbar and 620 °C, as $M(H_2O)$ becomes progressively undersaturated below ~5.25 mol%, the predicted abundance of garnet increases to as much as 30 vol% (Fig. 10c). At these very high degrees of undersaturation, the observed assemblage in MD20–06 can be effectively reproduced, though garnet rim compositions cannot be reproduced, and biotite modes, plagioclase modes, and H_2O contained in bulk solids reach values that are inconsistent with the observed rock volume (~12 vol%, 37 vol%, and ~ 0.3 wt%, respectively). Up-*T* open-system evolution of the system to well below H_2O saturation at the end of the low/medium pressure heating is therefore not considered likely.

6. Discussion

6.1. *Metamorphic evolution of the Loch Raven Schist*

Given the spatial proximity of MD20–06 and MD21–02, and the lack of preserved tectonic, deformational, or telescopic discontinuities separating the samples of Loch Raven Schist, we consider it most likely that both rocks experienced a common thermobarometric history. However, only through interrogating of both lithologies in tandem can the complete history be revealed. Taken together, the petrographic and geochronological assessment made in Loch Raven Schist samples from a single outcrop attest to a complex history of mid-Paleozoic heating and metamorphic reaction (Fig. 11). Simply, our data reveal: (1) an initial Silurian isobaric heating event at low-to-medium *P* (4.5–5.5 kbar; sil-stable) conditions; followed by (2) burial and heating to produce medium *P* (~8 kbar; ky-stable) metamorphism in the Devonian (Fig. 10).

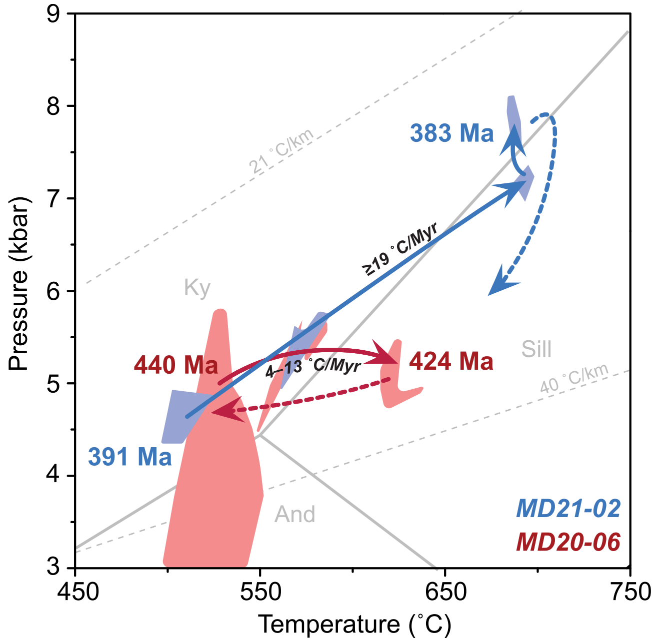

Fig. 11. Summary of equilibrium *P*–*T*–*t* evolution recorded in one outcrop of the Loch Raven Schist.

6.1.1. *Early (Silurian) low–medium pressure (sil-grade) regional metamorphism*

In samples MD21–02 and MD20–05, sillimanite inclusions in garnet cores attest to an early high *T*, low–medium *P* paragenesis (e.g., Holdaway, 1971). These are consistent with observations of sillimanite inclusions in garnet from Pennsylvania's Wissahickon Schist, the along strike equivalent of the Loch Raven Schist and which was metamorphosed at <4 kbar (Bosbyshell et al., 1999). Kyanite pseudomorphs after andalusite have also been reported at multiple Wissahickon localities (Crawford and Mark, 1982), as has unaltered andalusite (Crawford and Mark, 1982; Wyckoff, 1952). In contrast, in MD20–06, there are no aluminosilicate polymorphs and petrographic evidence of this event is elusive. However, phase equilibria modelling and independent thermometers applied to this low-Al bulk composition is consistent with the matrix and porphyroblastic assemblage in MD20–06 having formed at similarly low pressure peak conditions: *P* ~ 4.5–5.5 kbar and *T* ~ 620 °C (Fig. 9b, c).

Given these constraints, the period of pre-to-syntectonic garnet growth (and matrix deformation, given the garnet inclusion–matrix continuity) in MD20–06, with preferred ages between 440.2 ± 8.3 Ma and 423.0 ± 1.1 Ma, is interpreted to bracket the timing of a thermal peak during low–medium pressure metamorphism. Because of the spatial proximity of the two samples presented in this study (Fig. 2), the low-*P* inclusion phases in MD21–02 are also inferred to have formed at this time. Thermobarometry and garnet core–rim dates for MD20–06 require prograde heating rates for the early, sil-grade metamorphism on the order 4–13 °C/Myr.

Despite reaching elevated *T*, Silurian-aged garnet has not been identified in MD21–02. It may be that Silurian garnets grown along a low-*P* trajectory were not identified because of the bulk core–rim geochronology approach taken. However, the bimodal core–rim geochemical patterns and the well constrained multi-point isochrons yield little data spread, and investigation of outermost garnet rims reveal no chemical difference rim-wards of deflection planes. If garnet did crystallize as part of the stable assemblage in MD21–02 during this 440–424 Ma event, then it must have recrystallized, because we consider isotopic re-equilibration in the second event (given preservation of faster-diffusing Mn zoning) unlikely.

6.1.2. *Later (Devonian) medium-pressure (ky-grade) regional metamorphism*

Garnet core growth in MD21–02 at 391.5 ± 0.8 is interpreted to represent the first evidence for the transition to a distinct higher-*P* (ky-grade) metamorphic event. The rounded form of quartz inclusions in the cores of garnet compared to rims suggest this earliest garnet-forming reaction—at conditions of <400 °C and ~3 kbar (projecting the *P*–*T* path back to equilibrium garnet-in) or ~500 °C and ~4.5 kbar (isopleth intersection)—only partially consumed preexisting quartz associated with the earlier low-*P* paragenesis. The low abundance and absence of muscovite and chlorite, respectively, in garnet cores of MD21–02 is consistent with garnet formation via a chlorite, muscovite, and quartz consuming reaction (e.g., Farber et al., 2014), or these phases having been consumed during sillimanite-forming dehydration reactions in the earlier, Silurian metamorphic event.

The sharp core–rim boundaries exhibited in the microstructure, inclusion density, and trace element chemistry of MD21–02 garnets attest to a pronounced change along the Devonian heating trajectory presented in Fig. 9e. Observations of chemical and textural discontinuities in garnet from the Wissahickon of Pennsylvania were also made by Bosbyshell et al. (1999); in this case, cores were hypothesized as having been inherited during a low-*P* 'M2' event, and grossular-rich rims formed during a subsequent, medium-*P* 'M3' Acadian event. However, here we demonstrate that both garnet cores and rims in MD21–02 are Devonian. Moreover, REE zoning of garnet from both core to inner rim and the inner rim to the outer rim in MD21–02 (Fig. 6e, f) is consistent with partitioning during prograde garnet growth. The sharp and nonconcentric compositional step change between garnet cores and rims (best demarcated by Cr; Fig. 6d), may therefore have resulted from a reduction in garnet stability during prograde garnet-consuming reactions, potentially associated with staurolite growth (e.g., Pattison and Spear, 2018) modelled between ~625 °C and ~680 °C (point B to C2, Fig. 9d).

After resumption of garnet growth and crystallization of matrix sillimanite to conditions of 680–690 °C and ~7 kbar (Fig. 9d, e), garnet outer rim growth occurred at ~680–690 °C and 7.5–8.5 kbar in a kyanite-stable regime (point C2 to D, Fig. 5a). This phase of metamorphism is dated at 383.1 ± 1.0 Ma, indicating path-averaged prograde heating rates for the Devonian metamorphic event of ~20 °C/Myr. Peak kyanite-grade metamorphism exceeds the 540 °C and 6.1 kbar determined by Lang (1991) for the underlying Setters Formation.

Elevated grossular content in garnet rims is consistent with increased stabilization of low-Ca matrix plagioclase during up-*P* rim growth and some staurolite breakdown via a reaction that consumed more quartz than the initial garnet-forming reaction, accounting for the relative absence of quartz inclusions. REE increases outboard of the core-rim boundary may derive from trace element re-mobilization at renewal of fluid-oversaturated conditions at ~560 °C, producing fluid out of equilibrium with garnet cores that may also have driven secondary exsolution of fluid inclusions (Dempster et al., 2019). Interestingly, there is no evidence for remobilization of major elements associated with this change. The microstructural continuity between sillimanite included in staurolite and garnet rims and the sillimanite in the matrix (Fig. 4d), coupled with the presence of overprinting kyanite (Fig. 4a) suggests that mineral growth above ~7 kbar may have occurred after the cessation of the principal phase of deformation.

After peak-*P* conditions, a second, medium-*P* population of Acadian sillimanite was stabilized in MD21–02 on decompression (Fig. 9e). Sillimanite likely nucleated on kyanite as fibrolite needles at the margins of these porphyroblasts (Fig. 4g) owing to sluggish reaction kinetics associated with polymorphic transformations (Carmichael, 1969). During retrogression, fibrolite was partially replaced by white mica.

Because of the brief timescales required for thermal equilibration over short length scales of the sampling outcrop, peak temperature constraints of ~675 °C from MD21–02 are also considered to apply to MD20–06 at c. 391–383 Ma. Using the bulk composition of MD20–06 at the end of Silurian peak metamorphism, equilibrated re-metamorphism along the Acadian path would be expected to stabilize staurolite, at minimum (Fig. 10d). However, no evidence for a post-420 Ma paragenesis has been identified in the microstructure of MD20–06. In some garnet of MD20–06, ilmenite defines deflection planes that are continuous with the external foliation that were hypothesized to be a younger phase of garnet growth. However, these merge with the included fabric in some sections and their chemistry is continuous with that of the rest of the rim. Texturally, the outer garnet is therefore not considered to relate to a Devonian phase of growth and the matrix fabric is assumed to have formed approximately synchronously with c. 423 Ma rim growth. Additional geochronology of other metamorphic phases, including monazite, may yield additional insight into the relative (non-)reactivity of MD20–06 after the Silurian event.

6.2. *Implications for the tectonic evolution of the Central Appalachians*

6.2.1. *Ordovician–Silurian heating*

Our data present no evidence for Taconic metamorphism, in contrast to longstanding interpretations of the timing of regional metamorphism in the Baltimore Terrane (e.g., Aleinikoff et al., 2006; Sinha et al., 2012; Wagner and Srogi, 1987; Wise and Ganis, 2009). Instead, metapelites of the Loch Raven Schist attest to a significant mid-Silurian thermal anomaly at 440–424 Ma, starting 10–20 Myr after the end of proposed Taconic orogenesis in Baltimore and the central Piedmont (Horton Jr. et al., 1989; Sinha et al., 1997; Wise and Ganis, 2009).

These conditions of mid-Silurian, low–medium-*P* metamorphism in the Loch Raven Schist are remarkably similar to partially-preserved (and similarly-elusive) conditions determined in the type Wissahickon rocks surrounding the intrusive Wilmington Complex in Delaware (see Bosbyshell et al., 2016). TIMS and SHRIMP U–Pb monazite dates of 425.0 ± 0.5 Ma in those low-pressure assemblages are comparable to the Silurian event thermal maximum in Baltimore (Aleinikoff et al., 2006). The distribution of metamorphic assemblages around the Wilmington Complex, (originally interpreted to represent a magmatic arc) meant that it was inferred as a heat source for metamorphism along very high geothermal gradients (Bosbyshell et al., 1999). However, refinement of the timing of arc magmatism in Delaware and Pennsylvania, to 480–475 Ma, means this significantly pre-dates the Silurian metamorphism (Aleinikoff et al., 2006).

In the Baltimore Terrane, the Gunpowder Granite and associated granitoids (427 ± 3 Ma: Sinha et al., 2012) are of a similar crystallization age to the Silurian metamorphism recorded in MD20–06. However, there is no evidence for spatial association between the low-*P* metamorphism and bodies of the Gunpowder Granite. Moreover, the late-metamorphic timing of the Gunpowder Granite is more consistent with the granitic magmatism being a result of heat sources responsible for the Silurian metamorphism rather than a primary driver. Field observations have shown that the Gunpowder Granite and its injection complex intrudes both the Baltimore Terrane and BMC-associated Ordovician (Taconic), peri-Laurentian arc units (Bel Air Belt of Crowley, 1976), apparently overprinting the interpreted obduction thrust (Crowley et al., 1976); this interpretation constrains obduction of the BMC and Bel Air Belt (onto the Baltimore Terrane) to ≥425 Ma. It is possible that both the Silurian metamorphism recorded by MD20–06 and melting associated with the Gunpowder Granite are associated with obduction of the peri-Laurentian ophiolite/arc terranes, though the near-isobaric nature of proposed metamorphism is not directly consistent with tectonic loading via obduction. A ≥ 425 Ma timing of obduction precludes any role for associated heating in the Devonian ky-grade regional metamorphism.

Alternatively, Silurian-age magmatism in Maryland and Virginia has also been proposed to derive from extension in a west-dipping subduction zone that formed after Ordovician Taconic collision, or slab delamination and extension associated with final accretion of peri-Gondwanan terranes (Bosbyshell, 2001; Bosbyshell et al., 2005; Sinha et al., 2012). In such cases, rifting or slab delamination and associated extension would yield high heat flows over crustal length scales that may reasonably account for regional low–medium *P* and high *T* metamorphism (Bosbyshell, 2001) at c. 15 km depth. The c. 20 Myr duration of low–medium *P* Silurian metamorphism and clustered emplacement of Silurian-aged mantle-derived mafic igneous rocks between 423 Ma and 438 Ma (Sinha et al., 1997, 2012) together support an early extensional geometry in the central Appalachians.

6.2.2. *Devonian Barrovian-type metamorphism*

To account for the Devonian recrystallisation/renewed heating recorded in MD21–02, dissipation of heat associated with maximum temperatures during the Silurian low-*P* metamorphism must have occurred within ~30 Myr, implying cooling rates of >3 °C/Myr. After cooling and renewed incipient garnet growth at c. 391 Ma, c. 383 garnet rims that likely just pre-date peak kyanite–sillimanite grade Barrovian-type metamorphism in the Loch Raven Schist suggests a significant phase of burial along a geothermal gradient of approximately 30 °C/kbar during the Acadian orogeny.

Metamorphism of this age and style is well known in southern New England (e.g., Lancaster et al., 2008; Robinson et al., 1998), where the effects of accretion of Avalonia are most pronounced. In contrast, the effects of overprinting by Acadian orogenesis in the central Appalachians have generally been considered negligible or even absent (e.g., Faill, 1998; Hibbard et al., 2010b), with high *P*/*T* metamorphism instead inferred to result from earlier, Taconic orogenesis and collision of the peri-Laurentian arcs with the Laurentian margin. Combined with results from monazite of the Wissahickon in Delaware and Pennsylvania (e.g., Bosbyshell et al., 2016), data presented here suggest this is unlikely to be the case. This is also consistent with evidence of Devonian cleavage development in the westerly Westminster Terrane (Wintsch et al., 2010) and post-Taconic metamorphism in the Smith River Allochthon of Virginia (Broadwell et al., 2019).

This proposed timing of Acadian metamorphism in the central Appalachians is remarkably similar to that of Acadian thickening in the northern Appalachians. Gatewood et al. (2015) dated amphibolite-facies garnet core growth at 380 ± 2 Ma and rim growth at 376 ± 1 Ma, in rift-to-drift cover sediments overlying Grenvillian basement domes (i.e., the Athens and Chester Domes). One interpretation of these results is that the central Appalachians experienced a post-Ordovician history akin to that of northern Appalachian tectonism and that the New York Promontory should not be considered a fundamental boundary within the orogen (e.g., Hibbard et al., 2010). Alternatively, Bosbyshell et al. (2016) proposed that the arc-related Wissahickon sediments in central Pennsylvania were originally part of the Taconic arc in New England and were translated by strike-slip deformation to their present location. There is abundant regional evidence for young (late Devonian and younger) dextral transcurrent motion along, for example, the Pleasant Grove and Rosemount Shear Zones in Maryland and Pennsylvania, respectively (e.g., Bosbyshell, 2001; Valentino et al., 1994). As much as 150 km of dextral displacement has been suggested for the Pleasant Grove Shear Zone, based in part on similarities between rock in New York and Baltimore (Valentino et al., 1995). The similarity in ages for crustal thickening in Maryland (this study) and Vermont (Gatewood et al., 2015) provides support for these interpretations.

6.3. *Heterogenous prograde reactivity*

Despite the relatively high temperatures reached in the Baltimore Terrane during the Devonian regional metamorphic event, sample MD20–06 appears to have been metamorphically unresponsive and preserves only Silurian paragenesis. In contrast, sample MD21–02 responded absolutely to the Devonian metamorphic episode and preserves evidence the Silurian metamorphism only in relict assemblages.

6.3.1. *Kinetic barriers to recrystallisation in MD20–06*

The dominantly Acadian assemblage in MD21–02 (and indeed much of the Baltimore Terrane cover sequence in which kyanite/sillimanite grade assemblages are documented) suggests this lithology was highly susceptible to recrystallisation after low/medium-*P* metamorphism. Dehydration associated with Silurian sillimanite formation in compositions equivalent to MD21–02 would have been synchronous with dehydration along the same *P*–*T* path in MD20–06. However, unlike the latter, the former did not yield a persistently unreactive assemblage that recrystallized almost all evidence for the former event during renewed metamorphism. To account for this difference in reactivity, we hypothesize that post-Silurian and pre-Acadian retrogression essentially primed MD21–02 for recrystallisation, as has been documented in numerous studies (e.g., Broadwell et al., 2019; Morrissey et al., 2016; Tenczer et al., 2006). It is well-known that reactions can be inhibited in the absence of a catalytic fluid (Baxter, 2003; Rubie, 1986). The presence of H_2O, even in concentrations of a few ppm can grossly enhance reaction rates (e.g., Milke et al., 2013; Rubie, 1986), trigger metastable reactions (e.g., Schorn and Diener, 2017), and act as a chemical component (e.g., Pattison et al., 2011), facilitating the continuous maintenance of near-equilibrium assemblages within the reactive bulk composition. So, breakdown of retrogressive hydrous phases and the liberation of H_2O in the initial stages of the Acadian thermal event ensures this domain would have remained reactive. Given this scenario, modelling of MD21–02 with an H_2O-undersaturated composition may be unnecessary. However, similarities in univariant topologies and discerned *P*–*T* evolution between H_2O undersaturated and oversaturated scenarios (Fig. 9) suggests the difference is insignificant.

There is no clear reason why a similar process should not have permeated the horizon of MD20–06, which may represent more psammitic primary depositional horizons of the Loch Raven Schist. Fluid infiltration and reworking may have been patchy and MD20–06 simply represents a small horizon that escaped these effects, potentially due to strain shielding or lithological/textural differences. While evidence for a strained contact is no longer present, these effects and later obscurement/overprinting of their textural signatures is possible. The litho-horizon likely experienced a mid-Silurian history of open system fluid loss related to the breakdown of hydrous phases (muscovite and chlorite), potentially akin to dehydration during sillimanite formation in MD21–02. Along this path, liberation of mineral-bound OH reduces the H_2O in solids from ~3.5% to 1.5 wt%, synchronous with the decline in the total molar volume of H_2O in the reactive bulk chemistry. MD20–06 lacks the typical evidence for low-T hydrous retrogression (e.g., chloritization) that might be expected at least to a minor degree, and instead preserves a relatively pristine Silurian assemblage. Taken together, this suggests that in the intervening c. 33 Myr between peak Silurian and incipient garnet-grade Devonian metamorphism, the assemblage was not subject to significant fluid ingress that primed the assemblage for recrystallization. Therefore, on renewed pressure increase in the Devonian, the relatively dry volume with ~1.5 wt% H_2O was subject to relatively sluggish reaction kinetics and failed to recrystallize new prograde equilibria (Fig. 10d) that would reset garnet chronometers. In addition, the large, refractory Silurian grains that make up 25–35 vol% of the rock and which have low surface area-to-volume ratio likely prevented their efficient dissolution. The resultant sequestering of garnet-forming components may have contributed to the enhanced metastability of the assemblage.

There are numerous examples of previously metamorphosed terranes that record little evidence of later high-*T* events, often in dry, relatively static granulitic terranes or those having experienced partial melting (e.g., Tenczer et al., 2006; Brown & Korhonen, 2009; Morrissey et al., 2016). In contact aureoles surrounding large intrusions with limited rock-scale deformation, petrological evidence of significant degrees of overstepping (50–70 °C) and persistent disequilibrium has also been established (e.g., Pattison and Tinkham, 2009; Waters and Lovegrove, 2002). In contrast, the generally more significant/pervasive deformation experienced by regional metamorphic settings is often inferred to preclude significant accumulation of disequilibrium: deformation facilitates accumulation of strain energy that may support the nucleation of new phases (e.g., George and Gaidies, 2017) and enhance overall reaction rates (e.g., Baxter and DePaolo, 2004). In MD20–06, the pronounced continuity between inclusions in c. 424 Ma rims of garnet and the external fabric suggests that post-peak Silurian deformation or deformation associated with early stages of Acadian metamorphism exerted little-to-no influence on the earlier-formed biotite-rich fabric. Thus, it is possible to infer limited accumulation of strain energy in mineral lattices after Silurian garnet growth, reducing the free-energy contribution to nucleation in the Acadian event by effects such as nucleation at dislocations or in domains of disordered structure as subgrain and grain boundaries are created and migrate. Coupled with the absence of catalyzing fluids, this limited deformation response may have erected significant kinetic barriers to Devonian recrystallization in bulk compositions equivalent to MD20–06.

Phase equilibria also suggest that following the Silurian event, the accumulated affinity (an empirical term describing the driving force of a reaction and, therefore, the maximum possible driving force for nucleation: Pattison et al., 2011) for garnet-formation during the secondary metamorphic event would be extremely high (Fig. 10d). Using the inherited peak-Silurian bulk composition of MD20–06 at the start of the Devonian, the initial affinity for renewed garnet nucleation at 500 °C and 4.5 kbar is extremely high: ~20 kJ/mol of 12 O garnet (~1.6 kJ/mol O in garnet calculated using the method of Pattison et al., 2011) at the conditions recorded by incipient garnet, increasing to >23 kJ/mol of garnet (nearly 2 kJ/mol O) at peak Devonian conditions (Fig. 10d).

Estimates of maximum affinity at conditions of overstepped nucleation in metapelitic systems vary significantly, from 166 J/mol O (Wilbur and Ague, 2006; George and Gaidies, 2017) and 281 J/mol O (Lanari and Duesterhoeft, 2019), to 500 J/mol O (Pattison et al., 2011), but our estimates of affinity in MD20–06 are substantially higher. If these estimates are reasonable (and we have no reason to believe they are not), the lack of Acadian garnet in MD20–06 implies the barriers to crystallization arose from limited fluid availability, lack of strain accumulation, and/or refractory assemblages must have been substantial and effectively precluded recrystallization.

6.3.2. *Diffusive records of episodic heating?*

Interestingly, the diffusive record of the high-*T* Devonian metamorphic event is also elusive in MD20–06. At the high temperatures and approximately 8 Myr duration of the Acadian overprinting, scaling relationships (e.g., Darken and Gurry, 1953) and thermal conductivities suggest that equilibration across scales of decimeters to kilometers should have occurred. Even if the discussed kinetic barriers locally precluded recrystallisation of the assemblage in MD20–06, the prolonged total period at high *T* might be expected to relax grain-scale gradients in major element zoning garnet at scales exceeding 100 μm (Ague and Baxter, 2007; Caddick et al., 2010; Viete et al., 2011). However, as discussed by Caddick et al. (2010), timescales for incipient resetting of garnets approximately 1 cm in diameter at conditions of c. 650–750 °C is 10^8–10^9 years, so for the large crystal sizes of this study (2–4 cm in MD20–06, and 4–7 mm in MD21–02), preservation of divalent cation zoning (Fig. 5c) is anticipated even at high sub-solidus temperatures. Similarly, the retention of REE growth zoning above closure temperatures of Sm—Nd in garnet is expected (e.g., Smit et al., 2013).

At conditions of the Acadian metamorphic event (550–700 °C over approximately 8 Myr), diffusion coefficients in garnet ($\log10^{-21}$–$\log10^{-24}$ m^2 s^{-1} for Fe and Mg; Carlson et al., 2006) would also be expected to yield centimeter-scale Fe—Mg exchange. However, he steep gradients in major element composition in garnet, over <100 μm (Fig. 5d) in the vicinity of biotite inclusions in MD20–06 are significantly less than expected for a composition that experienced the prolonged high T of the Acadian event. These observations may suggest that the Baltimore Terrane experienced a punctuated metamorphic history, consistent with models for Barrovian metamorphic heating suggested by Viete et al. (2013). In contrast to a regional heat source that developed continuously and incrementally, the thermal evolution may have derived from numerous short timescale heat sources whose separate thermal impacts were spatially limited, but which produced the seemingly typical regional metamorphism on the timescale recorded by garnet geochronology. In such a scenario, rocks with high self-affinity at the highest metamorphic grades responded to the broad episodic heating, but experienced only short timescales at near-peak temperature (Viete and Lister, 2017), accounting for the relatively limited degree of diffusional homogenization in garnet. In such a scenario, thermal anomalies would have been associated with transient rates of heating far exceeding the path-averaged ~20 °C/Myr.

7. Conclusions

The peak ~675 °C and 7.5–8.5 kbar conditions of widespread Barrovian metamorphism in Maryland's Loch Raven Schist, previously interpreted to have been driven by Taconic orogenesis, is markedly Acadian. This contributes to the expanding volume of evidence that mid-Devonian Acadian metamorphism—once thought to be restricted to the northern Appalachians (e.g., Hibbard et al., 2010)—is significant in the central–south Appalachians (e.g., Bosbyshell et al., 2016; Broadwell et al., 2019). Given similarities in the timing and conditions of metamorphism of analogous rift-to-drift cover sequences in the north (e.g., Gatewood et al., 2015), these results could suggest significant along-strike continuity of Avalonian collision, and that the New York promontory should not be considered the fundamental Appalachian boundary, or lend credence to proposals of orogen-scale dextral shear zones (Bosbyshell et al., 2016; Valentino et al., 1994). An >35 Myr older, c. 20 Myr-duration ~620 °C and 4.5–5.5 kbar thermal peak is also newly identified, and which may support a Silurian extensional geometry in the central Appalachians (Bosbyshell et al., 2007; Sinha et al., 2012). Discrepancies between the geochronologically-discerned timescales and the preservation of narrow diffusion profiles in garnet my allude to a punctuated high temperature thermal history.

However, our results demonstrate that this discerned history is heterogeneously preserved in metamorphic assemblages and mineral compositions: contrasting tectono-metamorphic and chronological histories in adjacent samples are juxtaposed across meter length scales. The bulk of the Baltimore Terrane's Loch Raven Schist records regional Barrovian-type Acadian metamorphism, with comprehensive recrystallization resulting in overprinting of all but cryptic mineralogical evidence for earlier Silurian metamorphism. The Silurian event is only fully preserved in spatially restricted locations, where a potential combination of paucity of post-peak fluid infiltration, limited strain accumulation, and/or coarse refractive assemblages stabilized an unreactive bulk rock composition. Having been documented in high-*T* granulites and associated with static contact aureoles, (e.g., Morrissey et al., 2016; Waters and Lovegrove, 2002) this work demonstrates that persistent metastability may also be an important phenomenon to consider in the context of the evolution/recrystallisation of mineral assemblages in amphibolite facies regional metamorphic terranes. In Baltimore, therefore, the full Paleozoic metamorphic evolution is only revealed given detailed outcrop-scale interrogation.

CRediT authorship contribution statement

Freya R. George: Writing – review & editing, Writing – original draft, Visualization, Validation, Methodology, Investigation, Funding acquisition, Formal analysis, Data curation, Conceptualization. **Daniel R. Viete:** Writing – review & editing, Visualization, Investigation, Funding acquisition. **George L. Guice:** Writing – review & editing, Investigation, Formal analysis. **Kayleigh M. Harvey:** Writing – review & editing, Methodology, Investigation. **Stephanie Walker:** Writing – review & editing, Validation, Resources, Methodology, Formal analysis. **Ethan F. Baxter:** Writing – review & editing, Resources, Methodology.

Declaration of Competing Interest

The authors declare that they have no known competing financial interests or personal relationships that could have appeared to influence the work reported in this paper.

Acknowledgements

Discussions with Jerry Burgess and Mark Caddick have been invaluable to the development of this work. Howell Bosbyshell and Laura Morrisey are thanked for thorough and constructive reviews that significantly improved this manuscript. Thanks also go to Nadia Malaspina for editorial handling. We acknowledge the financial (to FRG and DRV) and fellowship support (to FRG) from the Johns Hopkins Department of Earth & Planetary Sciences. LA–ICP–MS was supported by an NSF-EAR/IF grant (NSF-1831766) to DRV, and geochronology approaches (sample preparation and TIMS analyses) were supported by the Center for Isotope Geochemistry at Boston College.

Appendix A. Supplementary data

Supplementary data to this article can be found online at https://doi.org/10.1016/j.lithos.2024.107824.

References

Ague, J.J., Baxter, E.F., 2007. Brief pulses during mountain building recorded by Sr diffusion in apatite and multicomponent diffusion in garnet. Earth Planet. Sci. Lett. 261, 500–516.

Alcock, J.E., 1989. Tectonic Units in the Pennsylvania-Delaware Piedmont: Evidence from Regional Metamorphism and Structure. University of Pennsylvania.

Aleinikoff, J.N., Schenck, W.S., Plank, M.O., Srogi, L., Fanning, C.M., Kamo, S.L., Bosbyshell, H., 2006. Deciphering igneous and metamorphic events in high-grade rocks of the Wilmington Complex, Delaware: morphology, cathodoluminescence and backscattered electron zoning, and SHRIMP U-Pb geochronology of zircon and monazite. Geol. Soc. Am. Bull. 118 (1–2), 39–64.

Baxter, E.F., 2003. Natural constraints on metamorphic reaction rates. In: Vance, Muller, Villa (Eds.), Geochronology - Linking the Isotopic Record with Petrology and Textures, 220. Geological Society of London, Special Publication, pp. 183–202.

Baxter, E.F., Caddick, M.J., 2013. Garnet growth as a proxy for progressive subduction zone dehydration. Geology 41 (6), 643–646.

Baxter, E.F., DePaolo, D.J., 2004. Can metamorphic reactions proceed faster than bulk strain? Contrib. Mineral. Petrol. 146, 657–670.

Baxter, E.F., Caddick, M.J., Dragovic, B., 2017. Garnet: a rock-forming mineral petrochronometer. Rev. Mineral. Geochem. 83 (1), 469–533.

Bosbyshell, H., 2001. Thermal Evolution of a Convergent Orogen: Pressure-Temperature-Deformation-Time Paths in the Central Appalachian Piedmont of Pennsylvania and Delaware. Bryn Mawr College.

Bosbyshell, H., Crawford, M.L., Srogi, L., Valentino, D.W., Gates, A.E., 1999. The distribution of overprinting metamorphic mineral assemblages in the Wissahickon Group, southeastern Pennsylvania. Geol. Soc. Am. Spec. Pap. 41–58.

Bosbyshell, Howell, Aleinikoff, J.N., Blackmer, G.C., 2005. A Silurian age for the springfield granodiorite: tectonic and metamorphic implications for the central Appalachian piedmont. Geol. Soc. Am. Abstr. Programs 37 (1), 65.

Bosbyshell, H., Srogi, L., Pyle, J.M., Blackmer, G.C., 2007, December. Preliminary monazite U-Th-total Pb absolute age constraints on crustal thickening and Siluro-Devonian dextral transpression: central Appalachian Piedmont, SE Pennsylvania. In: AGU Fall Meeting Abstracts, 2007. V23C-1555.

Bosbyshell, H., Srogi, L., Blackmer, G.C., Schenck, W.S., Mathur, R., Valencia, V., 2015. The tectono-thermal evolution of the central Appalachian Orogen: accretion of a peri-Gondwanan(?) Ordovician arc. In: Brezinski, D.K., Halka, J.P., Ortt Jr., R.A. (Eds.), Tripping from the Fall Line: Field Excursions for the GSA Annual Meeting, Baltimore, 2015, vol. 40. Geological Society of America Field Guide, pp. 35–59.

Bosbyshell, H., Srogi, L., Blackmer, G.C., 2016. Monazite age constraints on the tectono-thermal evolution of the central Appalachian Piedmont. Am. Mineral. 101 (8), 1820–1838.

Broadwell, K.S., Caddick, M.J., Beard, J.S., 2019. Polymetamorphism in high-T metamorphic rocks: an example from the Central Appalachians. J. Metamorph. Geol. 37 (9), 1209–1234.

Brown, M., Kothonen, F.J., 2009. Some remarks on melting and extreme metamorphism of crustal rocks. In: Physics and Chemistry of the Earth's interior: Crust, Mantle and Core. Springer New York, New York, NY, pp. 67–87.

Caddick, M.J., Konopásek, J., Thompson, A.B., 2010. Preservation of garnet growth zoning and the duration of prograde metamorphism. J. Petrol. 51 (11), 2327–2347.

Carlson, W.D., 2006. Rates of Fe, Mg, Mn, and Ca diffusion in garnet. American Mineralogist 91 (1), 1–11.

Carmichael, D.M., 1969. On the mechanism of prograde metamorphic reactions in quartz-bearing pelitic rocks. Contrib. Mineral. Petrol. 20, 244–267.

Crawford, M.L., Mark, L.E., 1982. Evidence from metamorphic rocks for overthrusting. Can. Mineral. (Pennsylvania Piedmont, USA) 20 (3), 333–347.

Crowley, W.P., 1976. The Geology of the Crystalline Rocks near Baltimore and its Bearing on the Evolution of the Eastern Maryland piedmont.

Crowley, W.P., Reinhardt, J., Cleaves, E.T., 1976. Geologic Map of the White Marsh Quadrangle, Maryland. Maryland Geological Survey. Scale 1:24,000.

Darken, L.S., Gurry, R.W., 1953. Physical Chemistry of Metals. New YorkMcGraw–Hill.

de Capitani, C., Petrakakis, K., 2010. The computation of equilibrium assemblage diagrams with Theriak/Domino software. Am. Mineral. 95 (7), 1006–1016.

Dempster, T.J., Gilmour, M.I., Chung, P., 2019. The partial equilibration of garnet porphyroblasts in pelitic schists and its control on prograde metamorphism, Glen Roy, Scotland. J. Metamorph. Geol. 37 (3), 383–399.

Dennis, A.J., Wright, J.E., 1997. The Carolina terrane in northwestern South Carolina, USA: late Precambrian-Cambrian deformation and metamorphism in a peri-Gondwanan oceanic arc. Tectonics 16 (3), 460–473.

Faill, R.T., 1998. A geologic history of the north-Central Appalachians: part 3, the Alleghanian Orogeny. Am. J. Sci. 298, 131–179.

Farber, K., Caddick, M.J., John, T., 2014. Controls on solid-phase inclusion during porphyroblast growth: insights from the Barrovian sequence (Scottish Dalradian). Contrib. Mineral. Petrol. 168, 1–17.

Fisher, G.W., Higgins, M.W., 1979. Geological Interpretations of Aeromagnetic Maps of the Crystalline Rocks in the Appalachians, Northern Virginia to New Jersey.

Fisher, G.W., Olsen, S.N., 2004. The Baltimore gneiss domes of the Maryland Piedmont. Geol. Soc. Am. Spec. Pap. 380, 307–320.

Forshaw, J.B., Pattison, D.R., 2023. Major-element geochemistry of pelites. Geology 51 (1), 39–43.

Gatewood, M.P., Dragovic, B., Stowell, H.H., Baxter, E.F., Hirsch, D.M., Bloom, R., 2015. Evaluating chemical equilibrium in metamorphic rocks using major element and Sm–Nd isotopic age zoning in garnet, Townshend Dam, Vermont, USA. Chem. Geol. 401, 151–168.

George, F.R., Gaidies, F., 2017. Characterisation of a garnet population from the Sikkim Himalaya: insights into the rates and mechanisms of porphyroblast crystallisation. Contrib. Mineral. Petrol. 172 (7), 57.

Harvey, J., Baxter, E.F., 2009. An improved method for TIMS high precision neodymium isotope analysis of very small aliquots (1–10 ng). Chem. Geol. 258 (3–4), 251–257.

Harvey, K.M., Walker, S., Starr, P.G., Penniston-Dorland, S.C., Kohn, M.J., Baxter, E.F., 2021. A mélange of subduction ages: constraints on the timescale of shear zone development and underplating at the subduction interface, Catalina Schist (CA, USA). Geochem. Geophys. Geosyst. 22 (9) e2021GC009790.

Hatcher, R.D., Tollo, R.P., Bartholomew, M.J., Hibbard, J.P., Karabinos, P.M., 2010. The Appalachian orogen: a brief summary. In: From Rodinia to Pangea: The Lithotectonic Record of the Appalachian Region, 206. Geological Society of America Memoir, pp. 1–19.

Hellstrom, J., Paton, C., Woodhead, J., Hergt, J., 2008. Iolite: software for spatially resolved LA-(quad and MC) ICPMS analysis. In: Mineralogical Association of Canada Short Course Series, 40, pp. 343–348.

Henry, D.J., Guidotti, C.V., Thomson, J.A., 2005. The Ti-saturation surface for low-to-medium pressure metapelitic biotites: implications for geothermometry and Ti-substitution mechanisms. Am. Mineral. 90 (2–3), 316–328.

Hibbard, J., 1994. Kinematics of Acadian deformation in the northern and Newfoundland Appalachians. J. Geol. 102 (2), 215–228.

Hibbard, J.P., van Staal, C.R., Miller, B.V., 2007. Links among Carolinia, Avalonia, and Ganderia in the Appalachian Peri-Gondwanan Realm.

Hibbard, J.P., van Staal, C.R., Rankin, D.W., Tollo, R.P., Bartholomew, M.J., 2010. Comparative analysis of the geological evolution of the northern and southern Appalachian orogen: late Ordovician-Permian. In: From Rodinia to Pangea: The Lithotectonic Record of the Appalachian Region, 206(03). Geological Society of America Memoir, pp. 51–69.

Holdaway, M., 1971. Stability of andalusite and the aluminum silicate phase diagram. Am. J. Sci. 271 (2), 97–131.

Holdaway, M.J., 2000. Application of new experimental and garnet Margules data to the garnet-biotite geothermometer. Am. Mineral. 85 (7–8), 881–892.

Holland, T.J.B., 2018. AX62: A Program to Calculate Activities of Mineral End-Members from Chemical Analyses. Retrieved from. https://filedn.com/lU1GlyFhv3UuXg5E9dbnWFF/TJBHpages/ax-.html.

Holland, T.J.B., Powell, R.T.J.B., 1998. An internally consistent thermodynamic data set for phases of petrological interest. J. Metamorph. Geol. 16 (3), 309–343.

Holland, T., Powell, R., 2003. Activity–composition relations for phases in petrological calculations: an asymmetric multicomponent formulation. Contrib. Mineral. Petrol. 145, 492–501.

Holland, T.J.B., Powell, R., 2011. An improved and extended internally consistent thermodynamic dataset for phases of petrological interest, involving a new equation of state for solids. J. Metamorph. Geol. 29 (3), 333–383.

Horton Jr., J.W., Drake Jr., A.A., Rankin, D.W., 1989. Tectono-stratigraphic terranes and their Paleozoic boundaries in the central and southern Appalachians. In: Dallmeyer, R.D. (Ed.), Terranes in the Circum-Atlantic Paleozoic Orogens: Geological Society of America Special Paper, 230, pp. 213–245.

Hughes, K.S., Hibbard, J.P., Miller, B.V., Pollock, J.C., Terblanche, A.A., Nance, D.M., Lewis, D.J., 2014. Does the Chopawamsic Fault Represent the Main Iapetan Suture in the Southern Appalachians? Geology, Geochemistry, and Geochronology of the Western Piedmont of Northern Virginia.

Kavage Adams, Rebecca, Junkin, William, Brezinski, David K., 2020. Accreted forearc, continental, and oceanic rocks of Maryland's Eastern Piedmont: The Potomac terrane, Baltimore terrane, and Baltimore Mafic Complex. In: Swezey, Christopher S., Carter, Mark W. (Eds.), Geology Field Trips in and around the U.S. Capital.

Lanari, P., Duesterhoeft, E., 2019. Modeling metamorphic rocks using equilibrium thermodynamics and internally consistent databases: Past achievements, problems and perspectives. Journal of Petrology 60 (1), 19–56.

Lancaster, P.J., Baxter, E.F., Ague, J.J., Breeding, C.M., Owens, T.L., 2008. Synchronous peak Barrovian metamorphism driven by syn-orogenic magmatism and fluid flow in southern Connecticut, USA. J. Metamorph. Geol. 26 (5), 527–538.

Lang, H.M., 1991. Quantitative interpretation of within-outcrop variation in metamorphic assemblage in staurolite-kyanite-grade metapelites, Baltimore, Maryland. Can. Mineral. 29 (4), 655–671.

Lang, H.M., 1996. Pressure-temperature-reaction history of metapelitic rocks from the Maryland Piedmont on the basis of correlated garnet zoning and plagioclase-inclusion composition. Am. Mineral. 81 (11–12), 1460–1475.

Macdonald, F.A., Ryan-Davis, J., Coish, R.A., Crowley, J.L., Karabinos, P., 2014. A newly identified Gondwanan terrane in the northern Appalachian Mountains: implications for the Taconic orogeny and closure of the Iapetus Ocean. Geology 42 (6), 539–542.

Martin, A.J., Bosbyshell, H., 2019. Further detrital zircon evidence for peri-Gondwanan blocks in the central Appalachian Piedmont Province, USA. Can. J. Earth Sci. 56 (10), 1061–1076.

McDonough, W.F., Sun, S.S., 1995. The composition of the Earth. Chemical geology 120 (3-4), 223–253.

Milke, R., Neusser, G., Kolzer, K., Wunder, B., 2013. Very little water is necessary to make a dry solid silicate system wet. Geology 41 (2), 247–250.

Morrissey, L.J., Hand, M., Kelsey, D.E., Wade, B.P., 2016. Cambrian high-temperature reworking of the Rayner–Eastern Ghats terrane: constraints from the northern Prince Charles Mountains region, East Antarctica. J. Petrol. 57 (1), 53–92.

Olsen, S.N., 1977. Origin of the Baltimore gneiss migmatites at Piney Creek, Maryland. Geol. Soc. Am. Bull. 88 (8), 1089–1101.

Palin, R.M., Weller, O.M., Waters, D.J., Dyck, B., 2016. Quantifying geological uncertainty in metamorphic phase equilibria modelling; a Monte Carlo assessment and implications for tectonic interpretations. Geosci. Front. 7 (4), 591–607.

Paton, C., Hellstrom, J., Paul, B., Woodhead, J., Hergt, J., 2011. Iolite: freeware for the visualisation and processing of mass spectrometric data. J. Anal. At. Spectrom. 26 (12), 2508–2518.

Pattison, D.R., Spear, F.S., 2018. Kinetic control of staurolite–Al2SiO5 mineral assemblages: implications for Barrovian and Buchan metamorphism. J. Metamorph. Geol. 36 (6), 667–690.

Pattison, D.R.M., Tinkham, D.K., 2009. Interplay between equilibrium and kinetics in prograde metamorphism of pelites: an example from the Nelson aureole, British Columbia. J. Metamorph. Geol. 27 (4), 249–279.

Pattison, D.R., De Capitani, C., Gaidies, F., 2011. Petrological consequences of variations in metamorphic reaction affinity. J. Metamorph. Geol. 29 (9), 953–977.

Pollington, A.D., Baxter, E.F., 2011. High precision microsampling and preparation of zoned garnet porphyroblasts for Sm–Nd geochronology. Chem. Geol. 281 (3–4), 270–282.

Powell, R., Holland, T.J.B., 2008. On thermobarometry. J. Metamorph. Geol. 26 (2), 155–179.

Robinson, P., Tucker, R.D., Bradley, D., Berry IV, H.N., Osberg, P.H., 1998. Paleozoic orogens in New England, USA. Gff 120 (2), 119–148.

Rodgers, J., 1970. Tectonics of the Appalachians.

Rubie, D.C., 1986. The catalysis of mineral reactions by water and restrictions on the presence of aqueous fluid during metamorphism. Mineral. Mag. 50 (357), 399–415.

Schorn, S., Diener, J.F.A., 2017. Details of the gabbro-to-eclogite transition determined from microtextures and calculated chemical potential relationships. J. Metamorph. Geol. 35 (1), 55–75.

Schumacher, J.C., 1991. Empirical ferric iron corrections: necessity, assumptions, and effects on selected geothermobarometers. Mineralogical Magazine 55 (378), 3–18.

Sinha, A.K., Hanan, H.B., Wayne, D.M., 1997. Igneous and metamorphic U-Pb zircon ages from the Baltimore Mafic complex, Maryland Piedmont. In: Geological Society of America Memoir, 191, pp. 275–286.

Sinha, A.K., Thomas, W.A., Hatcher, R.D., Harrison, T.M., 2012. Geodynamic evolution of the central Appalachian orogen: geochronology and compositional diversity of magmatism from Ordovician through Devonian. Am. J. Sci. 312 (8), 907–966.

Smit, M.A., Scherer, E.E., Mezger, K., 2013. Lu–Hf and Sm–Nd garnet geochronology: chronometric closure and implications for dating petrological processes. Earth Planet. Sci. Lett. 381, 222–233.

Spear, F.S., Kohn, M.J., Cheney, J.T., Florence, F., 2002. Metamorphic, thermal, and tectonic evolution of Central New England. J. Petrol. 43 (11), 2097–2120.

Srogi, L., Lutz, T.M., 1997. Chemical variation in plutonic rocks caused by residual melt migration: implications for granite petrogenesis. In: Sinha, A.K., et al. (Eds.), The Nature of Magmatism in the Appalachian Orogen, Geological Society of America Memoir, 191, pp. 309–335.

Srogi, L., Wagner, M.E., Lutz, T.M., 1993. Dehydration partial melting and disequilibrium in the granulite-facies Wilmington complex, Pennsylvania-Delaware Piedmont. Am. J. Sci. 293, 405–462.

Starr, P.G., Broadwell, K.S., Dragovic, B., Scambelluri, M., Haws, A.A., Caddick, M.J., Smye, A.J., Baxter, E.F., 2020. The subduction and exhumation history of the Voltri Ophiolite, Italy: evaluating exhumation mechanisms for high-pressure metamorphic massifs. Lithos 376, 105767.

Tenczer, V., Powell, R., Stüwe, K., 2006. Evolution of H2O content in a polymetamorphic terrane: the Plattengneiss Shear Zone (Koralpe, Austria). J. Metamorph. Geol. 24 (4), 281–295.

Trupe, C.H., Stewart, K.G., Adams, M.G., Waters, C.L., Miller, B.V., Hewitt, L.K., 2003. The Burnsville fault: Evidence for the timing and kinematics of southern Appalachian Acadian dextral transform tectonics. Geological Society of America Bulletin 115 (11), 1365–1376.

Valentino, D.W., Gates, A.E., Glover III, L., 1994. Late Paleozoic transcurrent tectonic assembly of the central Appalachian Piedmont. Tectonics 13, 110–126.

Valentino, D.W., Valentino, R.W., Hill, M.L., 1995. Paleozoic transcurrent conjugate shear zones in the central Appalachian Piedmont of southeastern Pennsylvania. J. Geodyn. 19, 303–324.

van Staal, C.R., Whalen, J.B., Valverde-Vaquero, P., Zagorevski, A., Rogers, N., 2009. Pre-Carboniferous, episodic accretion-related, orogenesis along the Laurentian margin of the northern Appalachians. Geological Society, London, Special Publications 327 (1), 271–316.

Vermeesch, P., 2018. IsoplotR: a free and open toolbox for geochronology. Geosci. Front. 9 (5), 1479–1493.

Viete, D.R., Lister, G.S., 2017. On the significance of short-duration regional metamorphism. J. Geol. Soc. Lond. 174, 377–392.

Viete, D.R., Hermann, J., Lister, G.S., Stenhouse, I.A., 2011. The nature and origin of the Barrovian metamorphism, Scotland: diffusion length scales in garnet and inferred thermal time scales. J. Geol. Soc. Lond. 168, 115–132.

Viete, D.R., Oliver, G.J., Fraser, G.L., Forster, M.A., Lister, G.S., 2013. Timing and heat sources for the Barrovian metamorphism, Scotland. Lithos 177, 148–163.

Volkert, R.A., Aleinikoff, J.N., 2021. Tectonic history of the Grenville-age Trenton Prong inlier, Central Appalachians, USA: evidence from SHRIMP U–Pb geochronology. Can. J. Earth Sci. 58 (10), 1027–1039.

Wagner, M.E., Srogi, L., 1987. Early Paleozoic metamorphism at two crustal levels and a tectonic model for the Pennsylvania-Delaware Piedmont. Geol. Soc. Am. Bull. 99 (1), 113–126.

Waters, D.J., Lovegrove, D.P., 2002. Assessing the extent of disequilibrium and overstepping of prograde metamorphic reactions in metapelites from the Bushveld complex aureole, South Africa. J. Metamorph. Geol. 20 (1), 135–149.

White, R.W., Powell, R., Holland, T., Worley, 2000. The effect of TiO2 and Fe2O3 on metapelitic assemblages at greenschist and amphibolite facies conditions: mineral equilibria calculations in the system K_2O–FeO–MgO–Al_2O_3–SiO_2–H_2O–TiO_2–Fe_2O_3. J. Metamorph. Geol. 18 (5), 497–511.

White, R.W., Powell, R., Johnson, T.E., 2014. The effect of Mn on mineral stability in metapelites revisited: new a–X relations for manganese-bearing minerals. J. Metamorph. Geol. 32 (8), 809–828.

Wilbur, D.E., Ague, J.J., 2006. Chemical disequilibrium during garnet growth: Monte Carlo simulations of natural crystal morphologies. Geology 34 (8), 689–692.

Wintsch, R.P., Kunk, M.J., Mulvey, B.K., Southworth, C.S., 2010. 40Ar/39Ar dating of Silurian and late Devonian cleavages in lower greenschist-facies rocks in the Westminster terrane, Maryland, USA. Bulletin 122 (5–6), 658–677.

Wise, D.U., Ganis, G.R., 2009. Taconic Orogeny in Pennsylvania: a ~15–20 my Apennine-style Ordovician event viewed from its Martic hinterland. J. Struct. Geol. 31 (9), 887–899.

Wyckoff, D., 1952. Metamorphic facies in the Wissahickon schist near Philadelphia, Pennsylvania. Geol. Soc. Am. Bull. 63 (1), 25–58.